AN ABSTRACT OF THE THESIS OF

Frederick Kyle Herrera for the degree of Master of Science in Civil Engineering presented on March 16, 2022.

Title: Enhancing Detection of Marine Debris with Polarimetric Imagery

Abstract approved: _____

Christopher E. Parrish

Marine debris is a chronic and increasingly pervasive problem for coastal regions around the world. Debris poses environmental risks, threats to wildlife, and degradation of the natural environment. Recent research has shown the advantages of uncrewed aircraft systems (UAS) for detection and recognition of marine debris, including the ability to efficiently collect data over large stretches of coast. To date, most UAS imagery acquisition is performed with red-green-blue ("natural color") imagery only. Polarimetric imaging, which captures information on the polarization state of electromagnetic radiation received at the camera, in addition to purely spectral information, has been shown beneficial in detection of human-made objects. This thesis investigates the ability to improve detection of marine debris using polarimetric imagery (PI). It is shown that PI bands increase the information content above and beyond spectral (RGB) bands and aid in visual detection and recognition of marine debris. Additionally, results of supervised classification revealed that classification accuracy improves through inclusion of image bands derived from the polarimetric information. While commercially available PI cameras are still very new and not quite operationally ready for installation on UAS, follow-on research using PI cameras on UAS is anticipated to greatly facilitate operational use of this new technology for marine debris mapping and management.

Enhancing Detection of Marine Debris with Polarimetric Imagery

by
Frederick Kyle Herrera

A THESIS

submitted to

Oregon State University

in partial fulfillment of
the requirements for the
degree of

Master of Science

Presented March 16, 2022
Commencement June 2022

Master of Science thesis of Frederick Kyle Herrera presented on March 16, 2022.

APPROVED:

_____

Major Professor, representing Civil Engineering

_____

Co-Major Professor, representing Civil Engineering

_____

Head of the School of Civil and Construction Engineering

_____

Dean of the Graduate School

I understand that my thesis will become part of the permanent collection of Oregon State University libraries. My signature below authorizes release of my thesis to any reader upon request.

_____

Frederick Kyle Herrera, Author

ACKNOWLEDGEMENTS

I would like to sincerely thank Oregon State University and the National Oceanic and Atmospheric Administration (NOAA) for the opportunity to perform fascinating research in an effort to combat the increasingly pervasive issue of marine debris. The following people deserve special recognition and thanks:

- First and foremost, my parents Virginia & Roland, for the endless support over the years in a selfless pursuit to see me succeed to my fullest potential.
- My brothers, Ian & Geoff, for being steadfast examples in drive and perseverance for both personal and career endeavors.
- Chris Parrish, my co-advisor overseeing this research, for always taking the time to explain fully and guide wholeheartedly while allowing me to maintain full control of research direction.
- Pedro Lomónaco, my co-advisor overseeing coursework, for helping me find my footing in grad school and inspiring my choice to pursue research.
- My friends and colleagues at OSU for being genuinely passionate about life and science. Always willing to delve into deep theoretical discussion or light-hearted banter when the technical got too overbearing.
- The faculty along the way, whether in coursework or networking, for exuberating a love of knowledge and a desire to see the students succeed. I was thoroughly impressed with not only the quality of teaching, but also the compassion and intrigue I experienced.
- My NOAA project partners that pushed me to deliver on project requirements, participate in high-level discussions, and fully understand the science presented in this paper.
- Michael Starek and Jacob Berryhill from Texas A&M Corpus Christi for assisting in fieldwork data collection.
- My committee, for being involved in any way, shape, or form, to the fulfillment of my degree.

TABLE OF CONTENTS

Page

LIST OF FIGURES

Figure Page

LIST OF TABLES

Table Page

LIST OF APPENDICES

Appendix Page

LIST OF APPENDIX FIGURES

Figure Page

LIST OF APPENDIX TABLES

Table Page

1. Introduction

Marine debris accumulation plagues coastal areas worldwide and presents both immediate and long-term risks to humans and wildlife. The debris is any man-made, persistent solid material that either directly or indirectly ends up in the marine environment from land or ocean-based sources (Sheavly and Register, 2007; Pawar et al., 2016). Understanding spatial densities and distributions of marine debris in different regions, as well as the proportions of different debris types, and how these variables are changing over time is key to developing policies and directing resources for cleanup and mitigation efforts. To this end, NOAA's Office of Response and Restoration (OR&R) Marine Debris Program (MDP), the lead agency in the U.S. for addressing marine debris, maintains a Marine Debris Monitoring and Assessment Project (MDMAP), in which external partners and volunteers conduct periodic debris surveys (Opfer et al., 2012; Banford, 2013).

Marine debris surveys entail walking randomly-selected transects, searching for debris within a specified distance on either side of the transect centerline, and characterizing and recording debris items (Burgess et al., 2021). Recently, studies have documented the capability of uncrewed aircraft systems (UAS) to aid in marine debris detection and recognition (Brooke et al., 2015; Gonçalves et al., 2020; Taddia et al., 2021). Benefits of UAS for marine debris surveys include the ability to collect data rapidly, efficiently, and safely for large stretches of coast that might be inaccessible on foot. Additionally, automating the detection of debris items in UAS imagery may assist in reducing some of the subjectivity of the *in-situ* surveys and in providing contiguous data (sometimes called "wall-to-wall coverage"), in comparison to random transects.

To date, UAS data acquisition for marine debris projects has primarily included only red-green-blue (RGB) imagery. However, an emerging technology—namely, low-cost, commercially-available polarimetric imaging (PI) cameras—offers the promise of potentially improving detection and recognition of marine debris, due to its potential to distinguish between natural and human-made features. Polarization sensors reveal information about surface textures, shape, shading, and roughness, thus making it a valuable tool in both research and field applications (Tyo et al., 2006). Islam et al. (2019) found that unique signatures contained within polarimetric data reliably improved separation of man-made objects using supervised classification methods.

This study, however, did not utilize multiband combination of polarimetric and RGB data for analysis. Furthermore, Zhao et al. (2008) suggests that combining spectral and polarimetric information greatly enhances object detection and identification performance. They conclude that spectropolarimetric image analysis efficiently separates objects and background features. Though useful for determining surface characteristics, polarimetric sensor technology has rapidly evolved over the last three decades to fit an expansive scope of disciplines. Traditional employment of polarimetry ranges from atmospheric remote sensing to astronomy, to military target detection, and even biomedical diagnostics. It is a crucial technique for characterization of aerosol particles, discernment of circumstellar structures, detection of camouflaged military vehicles, and diagnostics for tissue measurements. The expansive list of applications includes agriculture, forensics, coastal management, robotic vision, and more as polarimetry's uses continue to develop each year (Snik et al. 2014).

Polarization is one key property of light along with intensity, wavelength, and coherence (Tyo et al., 2006). Light has five potential polarization states: natural (non-polarized), linearly polarized, partially polarized, circularly polarized, and elliptically polarized. Natural light becomes polarized when it reflects off a surface, and the resultant angle of polarization is parallel to that surface. The degree and orientation (angle) of polarization observed from object reflectance are affected by surface structure, texture, chemical composition, water content, and angle of incidence (Yan et al, 2020). Objects on land produce unique polarized signals during reflectance, and this idea forms the basis for evaluating the efficacy of polarimetry in marine debris detection.

PI cameras work by including sensors employing a combination of filters with different angular orientations. Specifically, chip sensors have been developed that are overlayed with specific filter orientations to capture both the degree and angle of polarization. A combination of pixel filters, arranged at angles of 0, 45, 90, and 135 degrees, are typically overlayed atop the sensor in repeating 2-pixel blocks as shown in Fig. 1. This combination of 2×2-pixel filter blocks is then extrapolated for the full sensor size. To characterize the polarization of light, measurements from all four angles of polarization are required. To achieve this for each pixel on the sensor requires an interpolation process where data from adjacent pixels is combined. This procedure is analogous to how data from adjacent red, green, and blue pixels is combined on color sensors to

produce RGB values for each pixel via a Bayer filter. Modern sensors, such as the Sony IMX250MZR used in this study, provide unique opportunities with a total payload of less than 100 grams, opening the door to UAS platform integration.

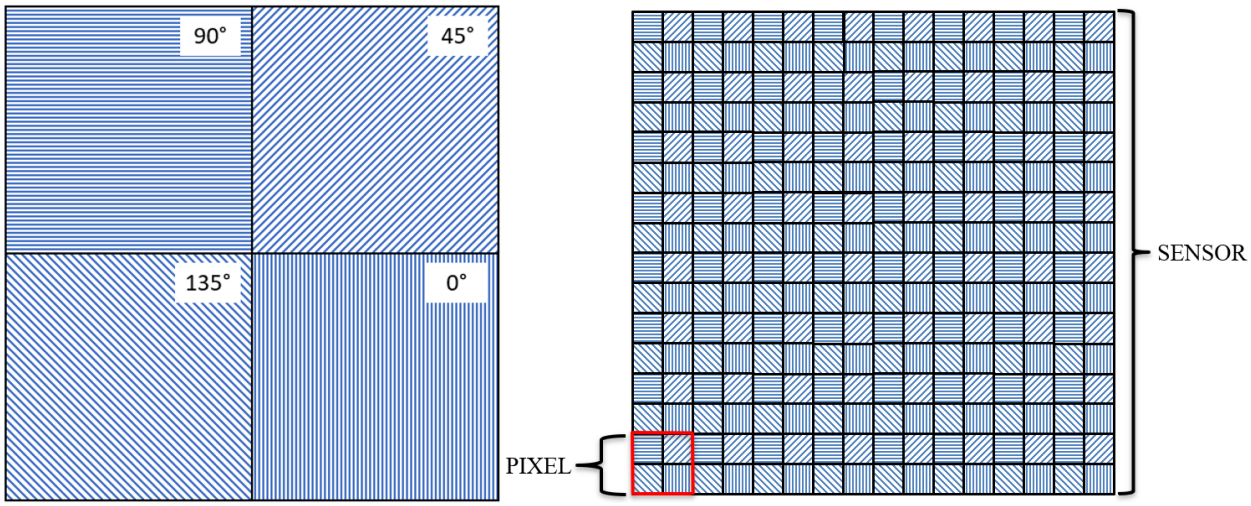

Figure 1: Polarizing filters overlaid on sensor in repeating pixel blocks (adapted from FLIR, 2021).

Despite the potential benefits of UAS-mounted polarimetric imaging cameras for marine debris detection and recognition, because affordable, commercially-available PI cameras are so new, this topic has not yet been studied. To that end, the goal of this thesis is to investigate and quantify potential improvement in marine debris detection and recognition using polarimetric imagery. The study utilized PI collected at four field sites and includes both visual and quantitative analysis. The visual analysis consists of viewing standard RGB imagery along with PI-derived image information to test whether the PI information improves detection of debris. Meanwhile the quantitative analysis includes both image band distance metrics (with the PI information treated as additional image bands) and supervised image classification, both with and without PI information included. The results indicate that PI information can, in fact, improve the detection of marine debris.

2. Methods

2.1. Equipment

Selection of a PI camera and development of the processing procedures were critical initial tasks in this study. The following sections detail the equipment and procedures.

The FLIR Blackfly S USB3 5-megapixel polarimetric camera was selected for use in this study to evaluate the efficacy of marine debris detection. It was paired with a Fujinon 12.5-mm focal length C-mount lens (Figure 2). The FLIR camera was secured to an extendable pole in all fieldwork scenarios to achieve the desired height above ground level. Two different poles were utilized, both outfitted with a 6.35-mm (¼") camera adapter for the FLIR to maintain nadir perspective. The first pole type was a plastic, extendable painter pole which secured to a weighted stand. The second was an extendable, metal survey rover pole which provided ample rigidity when extended to heights greater than 3.5m. This rigid configuration was essential for image quality when subjected to movement and wind gusts, which are common in many coastal locations. The pole was then either held by a crew member over debris object(s) or fixed in a weighted stand (Figure 3). The reason for operating the camera from a pole mount, rather than a UAS, in this research was that the lack of autonomous camera function meant that computer software was essential for not only saving images, but also adjusting the camera parameters. The camera required constant hardwired connection to the field laptop via a 5-m USB3.0 cable to perform any live parameter adjustments on the SpinView GUI (Teledyne Inc.) software, making it a two-person operation. The exposure settings were determined to be imperative for polarimetric quality, but needed to be changed frequently with changing illumination conditions (e.g. sun angle, clouds, shadows, etc.). These factors led to the need for meticulous manual adjusting of the PI camera parameters during acquisition.

Figure 2. (a-b) FLIR Blackfly S and Fujinon 12.5-mm focal length lens. (a) Camera and lens held in hand; (b) Camera and lens attached to pole.

Figure 3. (a-b) Camera configurations used in fieldwork scenarios. (a) fixed setup used at O.H. Hinsdale Wave Research Lab (left); (b) mobile setup used in Corpus Christi TX (right).

2.2. Processing Procedures

The first step in processing the data from the PI camera was to compute the Stokes parameters (Stokes, 1852), which describe the complete or partial polarization state of light. The Stokes vector, Eq. 1, consists of four parameters with three of them being mutually independent (Yan et al., 2020). The nature of these parameters is particularly well suited for the analysis of partially polarized light which is almost always observed in an outdoor environment (Snik et al., 2014). The four Stokes parameters, defined in Eq. 1, form the basis of all results generated in this study and serve as input to the calculations of the degree of linear polarization (DoLP) and the angle of linear polarization (AoLP). This four-dimensional vector can describe the status of any polarization state and degree (Yan et al., 2020):

$$S = \begin{bmatrix} S_0 \\ S_1 \\ S_2 \\ S_3^2 \end{bmatrix} = \begin{bmatrix} \langle \tilde{E}_x^2(t) \rangle + \langle \tilde{E}_y^2(t) \rangle \\ \langle \tilde{E}_x^2(t) \rangle - \langle \tilde{E}_y^2(t) \rangle \\ \langle 2\tilde{E}_x(t)\tilde{E}_y(t)cos\delta \rangle \\ \langle 2\tilde{E}_x(t)\tilde{E}_y(t)sin\delta \rangle \end{bmatrix} = \begin{bmatrix} I0 + I90 \\ I0 - I90 \\ I45 - I135 \\ 1 \ - (S1^2 + S2^2) \end{bmatrix} \quad (1)$$

where Ẽx and Ẽy are components of the electrical field vector along x, y in the selected coordinate system, δ is the phase differences between two vibration components, and ⟨⟩ denotes time-averaging.

The individual components of the Stokes vector are computed as shown in Eq. 2-6. First, intensity of non-polarized light, alternately denoted S_0 or I, is given by Eq. 2 and has a pixel value range of $0 \leq S_0 \leq 512$.

$$S_0 = I0 + I90 \quad (2)$$

The difference between horizontal and vertical polarized pixels is represented as S_1 (Eq. 3). Positive values are horizontally linearly polarized and negative values are vertically linearly polarized. The pixel value range associated is $-255 \leq S_1 \leq 255$.

$$S_1 = I0 - I90 \quad (3)$$

The 45-degree component is represented by S_2 (Eq 4) where positive values are 45° linearly polarized and negative ones are 135° linearly polarized. The pixel value range is similarly $-255 \leq S_2 \leq 255$.

$$S_2 = I45 - I135 \quad (4)$$

The final parameter, S_3, is the circular polarization component and is not measured by the IMX250MZR used in this study. S_3 is assumed to be zero because sunlight is unpolarized and its reflection only imparts linear polarization. However, in environments with controlled illumination it is possible to eliminate unpolarized light and characterize the circular component using Eq 5 (FLIR, 2021).

$$S_3^2 = 1 - (S_1^2 + S_2^2) \quad (5)$$

After computing the Stokes parameters, the next step is to compute the degree of linear polarization (DoLP) and angle of linear polarization (AoLP). DoLP is the primary means of interpreting polarization state and is represented by the proportion of light that is polarized at a given pixel. A completely unpolarized light source will have a DoLP of 0% while a perfectly polarized source would be 100%. This measure of intensity is represented by saturation level on a scale of zero to one, from white to black. DoLP is computed via Eq. 6 (Conte et al., 2021).

$$DoLP = P = \frac{\sqrt{{S_1}^2 + {S_2}^2}}{S_0} \quad (6)$$

The second component that describes the polarization status of light is the orientation or the angle of linear polarization (AoLP). In the AoLP calculation, Eq. 7, Ψ represents the azimuth angle of an eclipse based on the Stokes vector. The angle of polarization is often represented using a color wheel to denote specific orientation within a scene.

$$AoLP = \psi = \frac{1}{2}\, arctan\, (\frac{S_1}{S_2}) \quad (7)$$

Bivariate color maps can often display the association between two variables more effectively than a side-by-side comparison of the two individually (Trumbo, 1981). For visualization purposes, DoLP and AoLP are combined into a bivariate image which describes the polarization state in terms of hue and saturation, as shown in Fig. 4. Greater saturation (x-axis) corresponds to increasing degree of linear polarization while hue (y-axis) represents the angle of polarization at any given pixel.

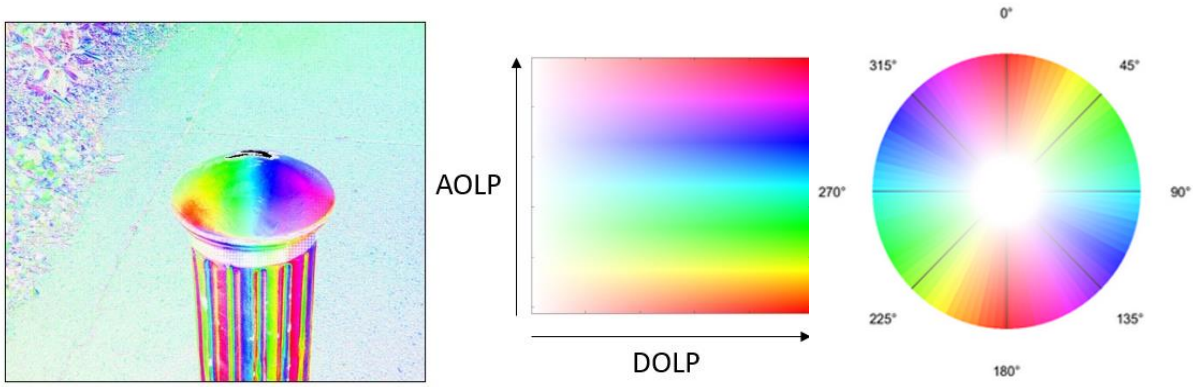

Figure 4. Illustration of bivariate image created from DoLP and AoLP. On the left is a bivariate DoLP/AoLP image of a pole in a walkway blocking vehicle traffic generated from imagery acquired with the camera used in this study. The plots on the right show how intensity, hue, and saturation are used to visually depict the degree and angle of linear polarization within the bivariate DoLP/AoLP image.

After computing the Stokes vector components and DoLP and AoLP, the next step was to bandstack the imagery to create multi-band images that included this additional PI-derived information as image bands. It should be noted here that there is no theoretical basis for treating *S*0, *S*1, *S*2, and *S*3 or DoLP and AoLP as "spectral" bands, and, in fact, they do not provide spectral information. However, treating the PI-derived information as additional bands enabled us to employ readily-available image analysis and classification routines and, thereby, to easily assess the potential improvement in marine debris detection and classification afforded by polarimetric information. The multi-band generation was performed in ArcGIS Pro v2.8.3 (Esri, Inc.). The analyses and classifications performed in this study utilized the polarimetric bands, *S*0, *S*1, *S*2, DoLP and AoLP, as additional spectral bands combined with standard RGB. This resulted in 8-band (R/G/B/S0/S1/S2/DoLP/AoLP) composite images for assessment purposes as portrayed in Fig. 5. There will naturally be some correlation between these bands, since, for example, DoLP and AoLP are computed from S0, S1, and S2. Hence, assessing band correlations and separability were part of the analysis.

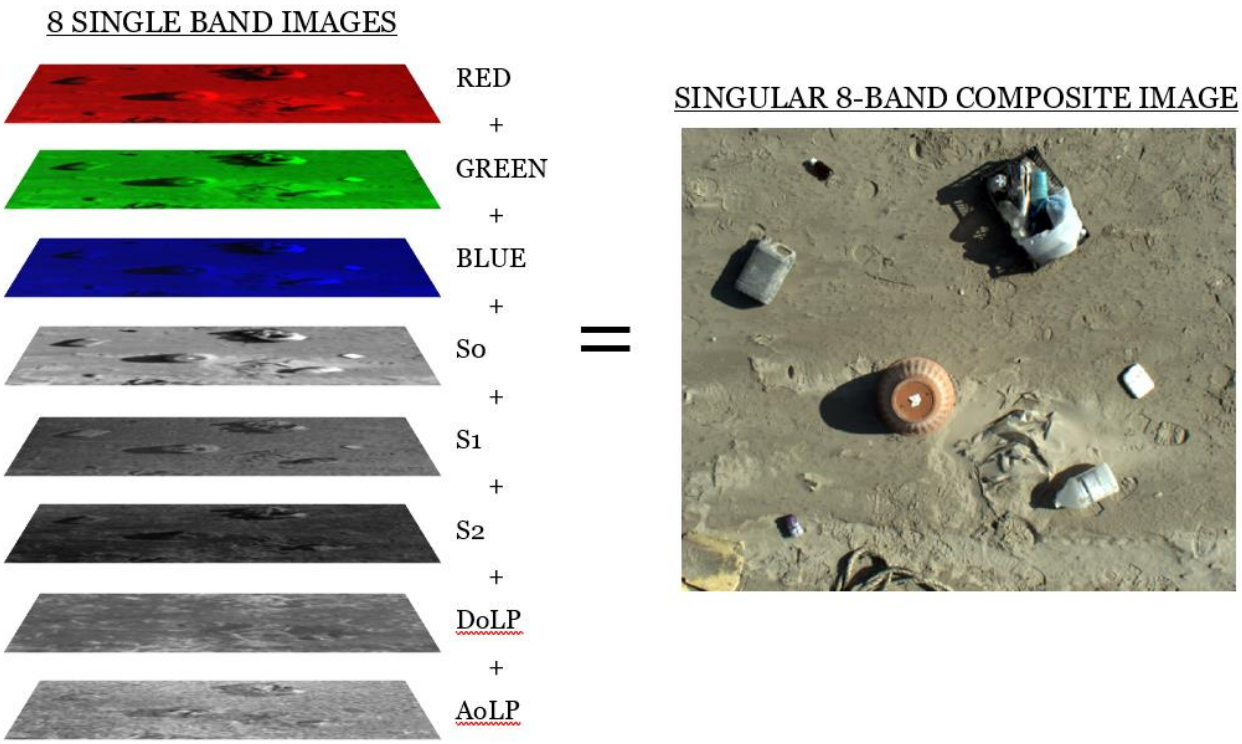

Figure 5. Visualization of the 8-band composite image generation in ArcGIS Pro, comprised of the R/G/B/S0/S1/S2/DoLP/AoLP layers.

Transformed Divergence (TD) is a prominent separability index in classification routines, representing the statistical difference between two multivariate, Gaussian distributed signatures (Chauhan, 2016). Idol et al. (2008), found that texture features extracted from polarization data greatly improved separability between land cover classes and overall classification accuracy. The Divergence (D) between two classes is shown in Eq. 9 and is used to compute the Transformed Divergence. TD has a value range of 0 to 2000, with 2000 being maximum spectral separability between classes, and is calculated as shown in Eq. 10. Mausel et al. (1990) concluded that TD is an excellent separability measurement for multi-band image classification and determining the best channel combinations.

$$D_{ij} = \frac{1}{2} tr[(C_i - C_j)(C_j^{-1} - C_j^{-1}) + \frac{1}{2} tr[(C_i^{-1} + C_j^{-1})(M_i - M_j)(M_i - M_j)^T] \quad (9)$$

where C is the class covariance matrix, M is the mean vector, and T is the transpose of the matrices.

$$TD_{ij} = 2000\,[1 - \exp\left(-\frac{D_{ij}}{8}\right)] \quad (10)$$

Band Correlation Matrices were also generated using ArcGIS Pro and used to assess the correlation between different image bands.

As the final step in the analysis, a supervised image classification was performed in MultiSpec (Biehl, 2002), both with and without the PI-derived bands included.

3. Experiment

3.1. Study Sites

PI imagery was acquired at a total of four different field locations, including a simulated beach at the O.H. Hinsdale Wave Laboratory on the Oregon State University campus (Figure 3a), Neptune State Scenic Area on the Oregon coast (Figure 5), and two areas on the Texas coast: Padre Island and San José Island, Figure 6. These sites were selected to achieve sufficient variability in not only material type and size, but also substrate and object state. Light sand, dark rock, and coastal vegetation are the foundation upon which many objects are typically found. Debris was encountered buried in, lying on top, or nestled within the various substrate types.

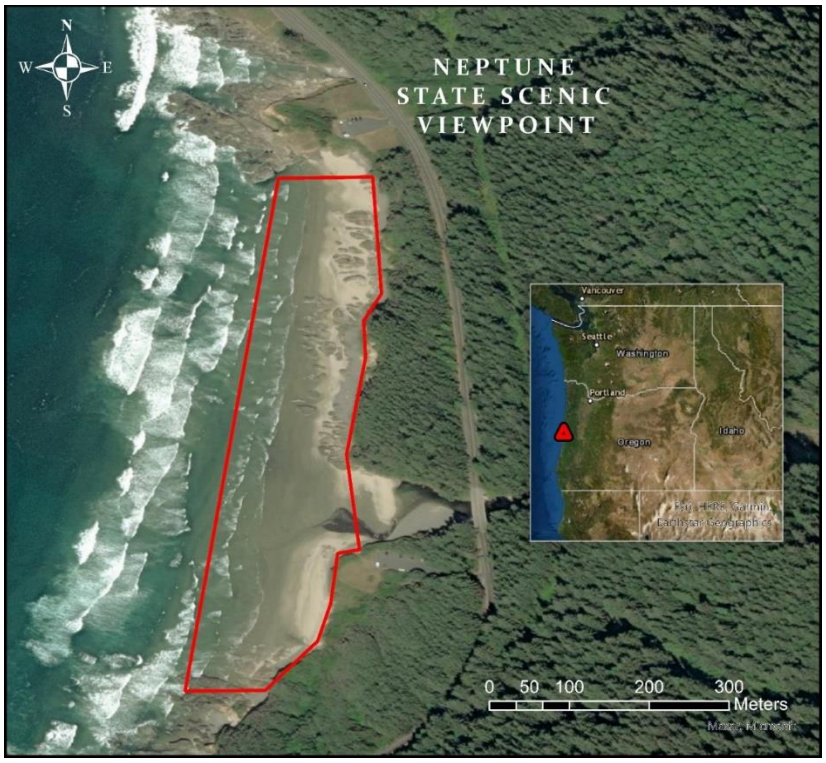

Figure 6. Neptune State Scenic Viewpoint AOI on the Oregon Coast.

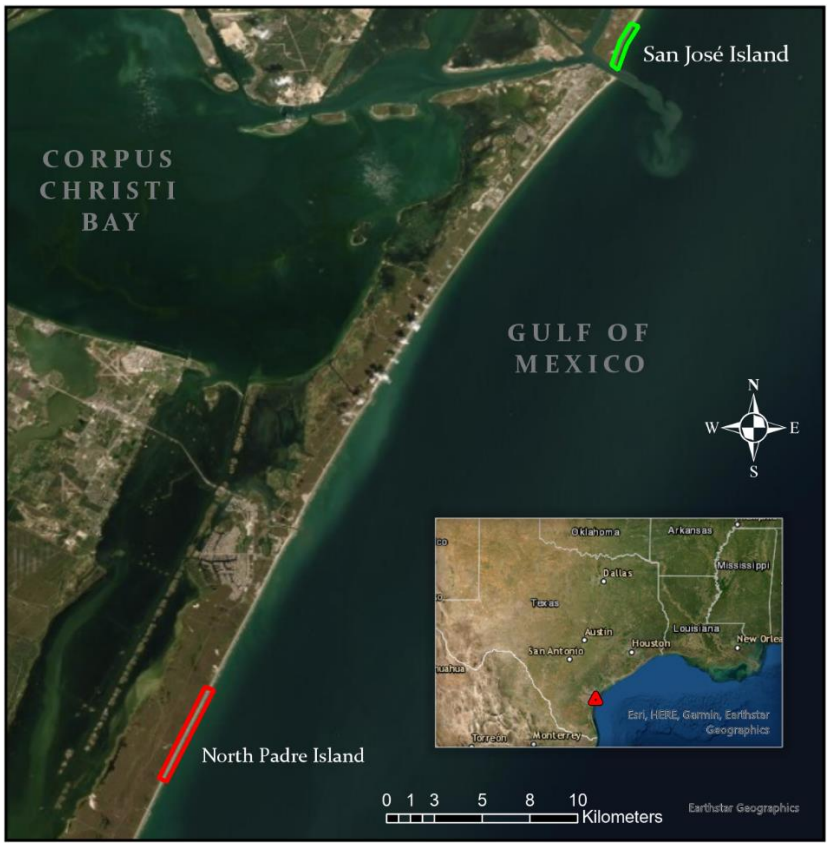

Figure 7. Corpus Christi Texas field sites.

The O.H. Hinsdale Wave Research Lab location contained sandy substrate (sourced from the Oregon coast) with direct sun exposure, making it a great scenario for initial camera testing and imagery acquisition. Debris utilized here consisted mostly of household debris objects, due to limited availability of actual shoreline debris. The round of testing conducted at this site served primarily as a proof of concept and provided a first look into polarimetric results. It was here that camera and software settings were tested and optimized, and above ground heights were explored.

The Neptune State Scenic Viewpoint located in coastal Oregon provided the first shoreline scenario for polarimetric image acquisition. It was here that procedures developed at the wave lab were translated to an actual beach. Due to the pristine nature of Oregon coastlines, the only *in-situ* debris readily observed are minimal microplastic fragments. Apart from storm events and select hotspots, weathered marine debris was surprisingly difficult to source. Oregon Parks and Recreation Department (OPRD) assisted in the gathering of actual debris objects that had

accumulated over time. This debris was transported by the OSU research team and hand-seeded along Neptune beach to simulate a debris-dense shoreline for polarimetric image acquisition.

The barrier islands east of Corpus Christi, located on the Texas Gulf Coast, featured a variety of *in-situ* macro debris objects, and included two sites well suited for validating the classification procedure. The beaches were flat, wide swaths of sand, about forty meters from the waterline to the backing dunes, with dense vegetation on the landward side. Site A, Padre Island, had debris focused along the seaward dune edge with debris objects partially buried in sand, due to the high wind conditions. Site B, San José Island, afforded substantial macro debris objects because of its remoteness and difficulty to clean. The debris here had a wider distribution along the beach width, ranging from the backside vegetation all the way to the waterline. Large storm events in previous years had washed ashore large objects such as vessels and metal mooring buoys. Most debris encountered between these two sites had been significantly weathered, making them excellent locations for evaluating operational capabilities under the challenging types of conditions encountered in marine debris surveys.

This experiment also investigated the potential applications for polarimetric sensors integrated on UAS platforms for marine debris management. With assistance from the US Coast Guard, the research team was able to simulate UAS altitudes to evaluate the camera performance by way of helicopter. Two tracks were flown over both study sites near Corpus Christi, TX. The camera was secured to a 1-m pole and held by hand outside of the cabin door, positioned nadir over the shoreline debris as shown in Figure 7. The first flight acquired imagery at 45-m altitude while the second achieved a 90-m flying height. The MH-65 helicopter maintained a speed of roughly 8 m/s and each flight strip produced 100 polarimetric images. The camera consistently captured quality imagery despite aircraft vibration and wind conditions. Objects on the ground exhibited valuable polarimetric returns from the elevations achieved, opening potential avenues for full UAS integration and debris management efforts.

Table 1 outlines fieldwork and data collection dates along with the objectives associated with each.

Figure 8. Polarimetric camera acquiring aerial imagery of debris at UAS altitudes onboard USCG helicopter.

3.2. Data Collection

Table 1. Description of the data collected at each of the study sites.

Date(s)	**Location**	**Equipment**	**Data collection objectives**
10/28/2020	O.H. Hinsdale Wave Lab	Fixed PI setup (2.1m AGL)	Obtain preliminary polarimetric results, test camera parameters
12/2/2020	O.H. Hinsdale Wave Lab	Fixed PI camera setup (3m AGL)	Test different material types and new sensor height
10/30-10/31/2021	O.H. Hinsdale Wave Lab	Fixed PI camera setup (3.7m AGL)	Test using actual marine debris sourced from Oregon coast at new sensor height, generate georeferenced orthomosaic
5/4/2021	Neptune State Scenic Viewpoint	Mobile PI setup (3m AGL)	Acquire polarimetric imagery of marine debris seeded on sandy shoreline
7/8/2021	Neptune State Scenic Viewpoint	Mobile PI setup (3.7m AGL)	Acquire polarimetric imagery of higher quality debris scene debris scene on mix of substrates (sand, cobble, rocky outcrop)
12/10/2021	Padre Island, TX	Mobile PI setup (4.4m AGL) w/ belt mount	Acquire polarimetric imagery of in-situ debris objects between 3 sections of shoreline

12/12/2021	San José Island, TX	Mobile PI setup (4.4m AGL) w/ belt mount	Setup robust debris field using debris sourced from 1km^2 area to create large orthomosaic analysis
12/14/2021	San José Island, TX	Mobile PI setup (5m AGL) w/ belt mount	Setup another debris field featuring different types of local debris objects for orthomosaic analysis
12/15/2021	Padre Island & San José Island, TX	FLIR attached to 1m pole, held out of cabin door	Fly over both Texas field sites with USCG support to test camera capabilities at UAS altitudes (45-90m AGL)

Of the data collection activities listed above, the data in the debris fields on San José Island, Texas, served as the primary data set for this research.

This study site was located within first couple kilometers north of the north Port Aransas jetty. The site contained a range of debris extending from water line up to the dune. The composition was mostly plastics, especially near the water, with some larger objects sprinkled up towards the dune line. The polarimetric imagery acquired in the site included a mix of singular frames with interesting/multiple objects as well as a constructed conglomerate scene using a substantial number of objects from several different classes.

The project team aggregated debris from a 1km^2 area to form two different debris fields, each containing different material types and distributions. The larger field was organized into a 38×8 m scene to achieve high quality polarimetric data of the native debris items (Fig. 8). The scene included mostly plastic objects ranging from water bottle size up to some larger gas jugs/barrel fragments. The next most populated classes in the scene were ropes (~12) and wood (~12). The ropes varied in length, diameter, and color, as did the wood samples. The smaller debris field accounted for alternate debris classes and allowed for rigorous analysis of rubber (tire fragments/flip flops), glass, wood, buoys/foam, and aluminum. This scene was more compact with an area of 6×2.5 m and is shown in Figure 10. These seven classes (plastic, rope/line/net, wood, rubber, glass, buoys/foam, and aluminum) had substantial sample size for robust testing to determine whether inclusion of polarimetric bands improved detection/classification of these types.

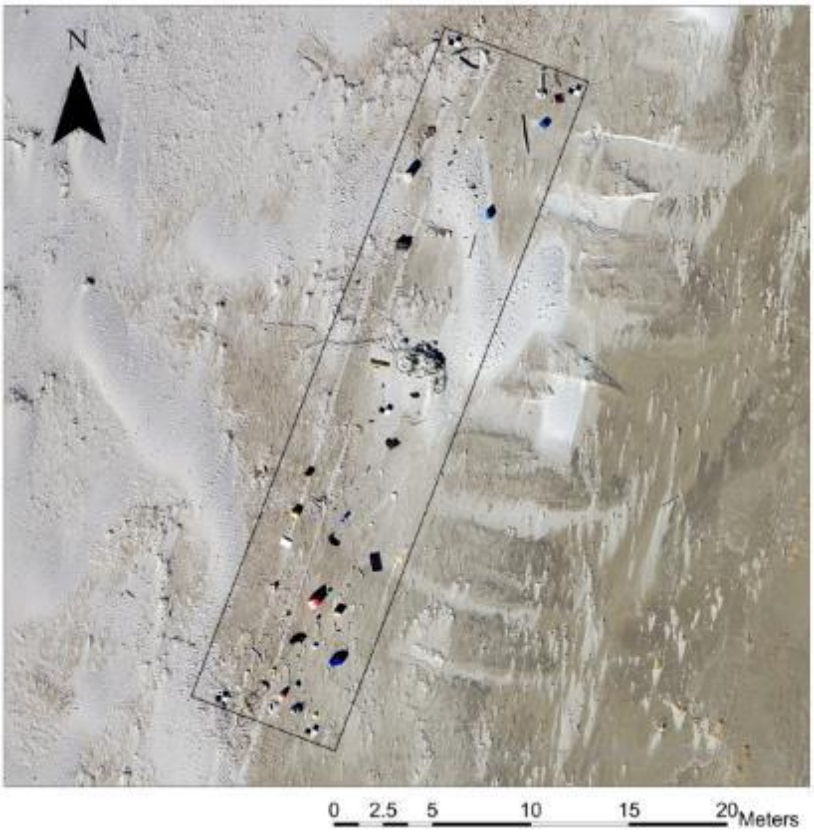

Figure 9. Debris Field 2 on San José Island.

Figure 10. Polarimetric imagery acquisition at San José debris field 2 on 12/12/2021.

After the bandstacking operation performed in ArcGIS to generate 8-band individual frame images, these images were then processed in Agisoft Metashape to generate georeferenced orthomosaics. The debris field orthomosaics served as input to the k-nearest neighbors (KNN) algorithm for supervised classification in MultiSpec. KNN was selected as the classification routine due to the simple yet effective employment in discriminant analysis (Silverman and Jones, 1989). To enable the comparison between the imagery with and without the PI-derived information included, the original three-band (RGB) images were also processed in Metashape to generate a separate set of orthomosaics. Objects within each scene were split into training and test fields, and each class contained 12-30 fields for evaluation. Objects were selected, based on the goals of having roughly equal numbers of each type and condition (weathered/new, partial/whole, color, size) of object in the training and test data sets. The model tested on the same samples it used for training, making the training accuracy improvement also noteworthy. The nearest K Neighbor value was set to 5 and the total run time was about 150 hours for the three scenes. Training and test accuracies as well as kappa statistics improved with inclusion of the polarimetric data stacked as additional spectral bands.

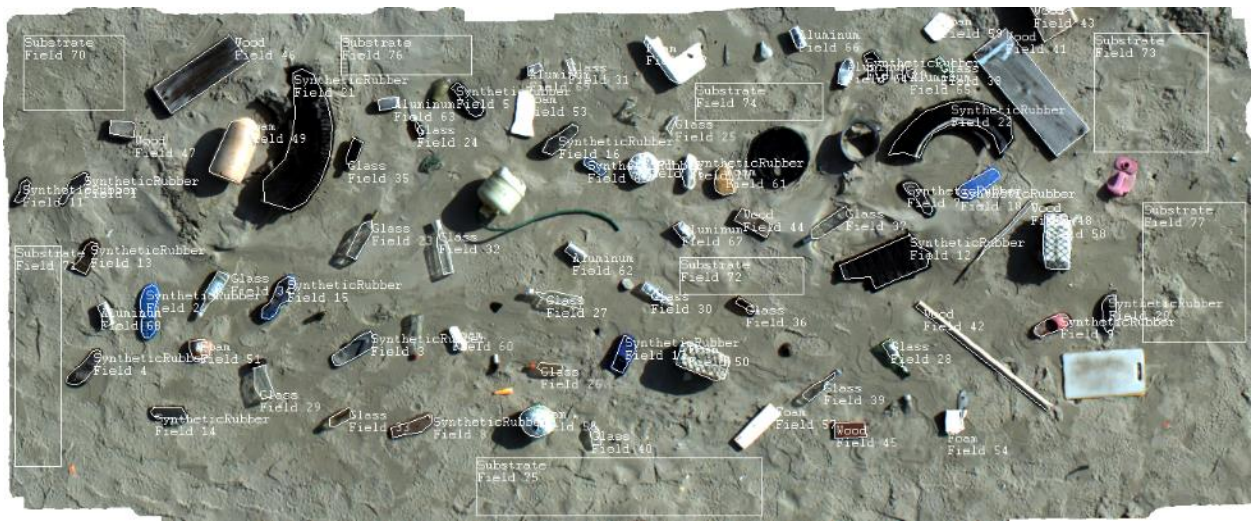

Figure 11. Object class sample fields selected in MultiSpec for supervised classification of San José orthomosaic 1.

4. Results

4.1. Visual Assessment

The first part of the analysis was to visually assess the PI camera outputs to see if they improved visual detection and recognition of debris over what is achievable with RGB imagery only. This visual representation was achieved using the bivariate display consisting of DoLP and AoLP measurements. It was found that PI is visually rich in the instance of like-color substrate and objects, dark scenes, structural perception, and material type distinction. Dark objects with distinct angular features are better perceived in the polarimetric display. Similarly, dark scenes where the object surfaces visually blend into the substrate are more easily distinguished in the polarimetric imagery. In instances of homogenous backgrounds such as fine sand, PI helps to highlight the shape of objects and allow for easier visual inference (natural vs man-made). As the substrate becomes more complex, including items such as shells, rocks, and vegetation, the visual quality of polarimetric imagery is diminished. At high elevations, man-made objects are still easily discernible in the polarimetric imagery when surrounded by sand or minimal vegetation. These observations are all represented in Figures 11-15 as well as Appendix A.

Material type and surface textures can be observed in Figure 11 with smooth, reflective objects (i.e., undamaged plastics and coated metal bars) showing the strongest polarimetric returns. Objects with granular surface textures, such as the bike tire, exhibited less specular reflectance (indicated by a “shiny” appearance in the RGB imagery) and had a lower degree of polarization. Against the dark rock backdrop, however, the circular tire shape is still visually discernable. Figure 12 displays *in-situ* examples of weathered and partially buried debris objects encountered at San José Island TX. Defining object characteristics, such as shape or texture, are readily observed in the bivariate display for the bucket, tire fragment, and rope despite the natural deformation to object state. The influence from complex substrate type can be seen in Figs 11-14 where rocks, shells, wood, and vegetation draw significant visual attention. Smooth sand has a uniform, dull appearance in the bivariate polarimetric imagery, allowing debris objects to readily stand out against a sand background. For example, in Fig. 13, man-made objects are readily discernable from natural sand in the imagery acquired over San José debris field 2 from 45-m altitude in the USCG helicopter.

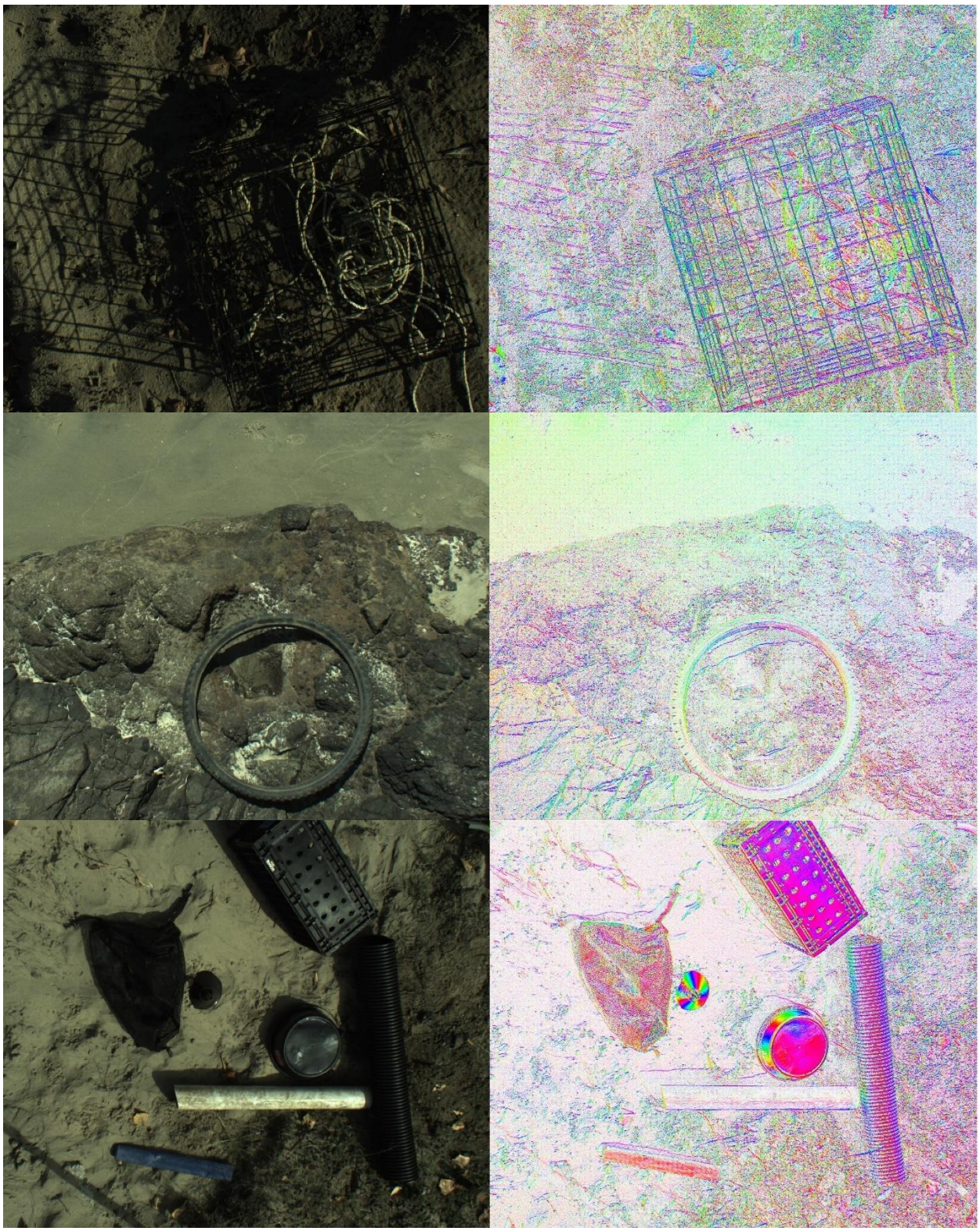

Figure 12. Various debris types over Oregon substrate. RGB image (left) vs Bivariate image (right).

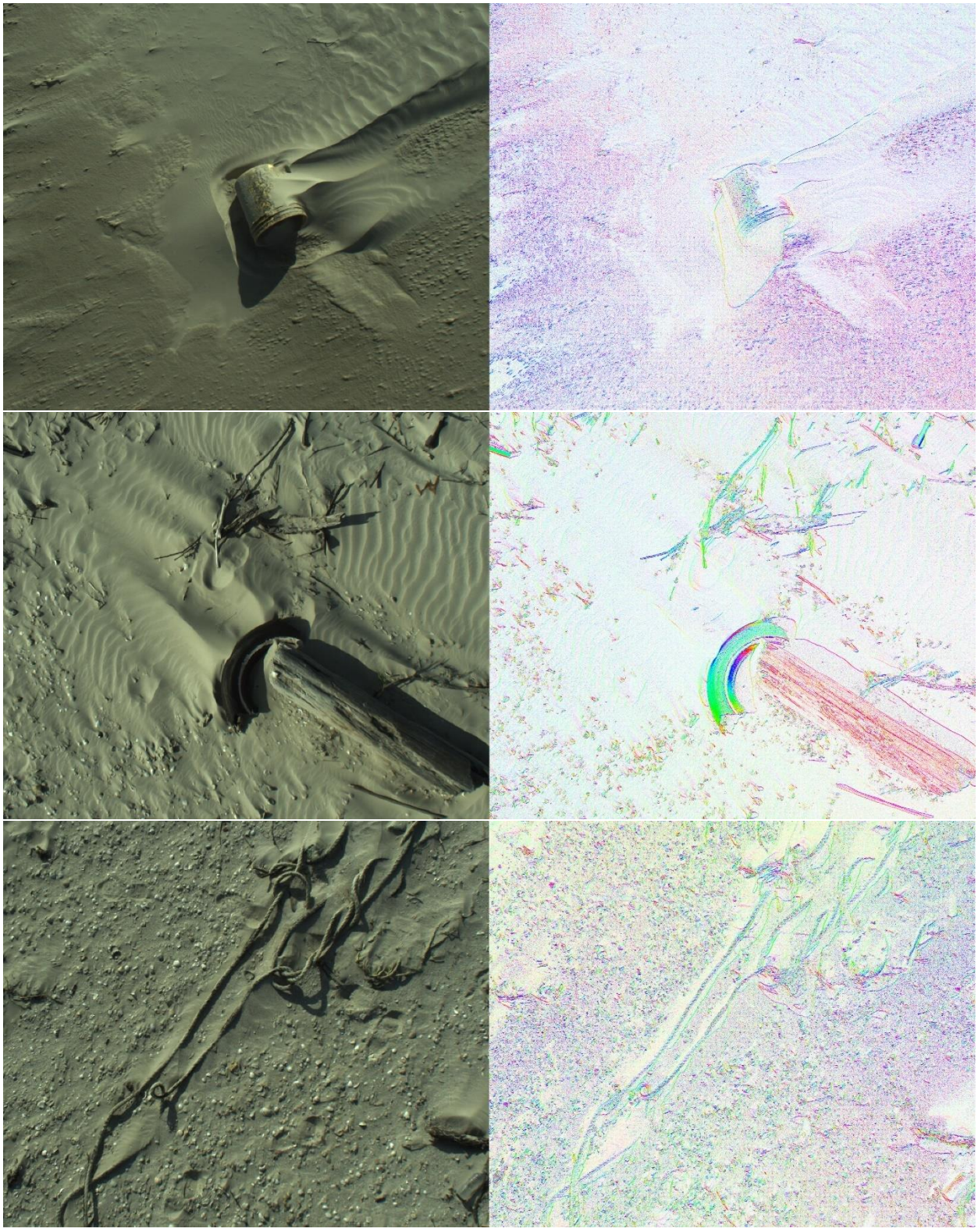

Figure 13. Partially buried debris objects at San José Island, TX.

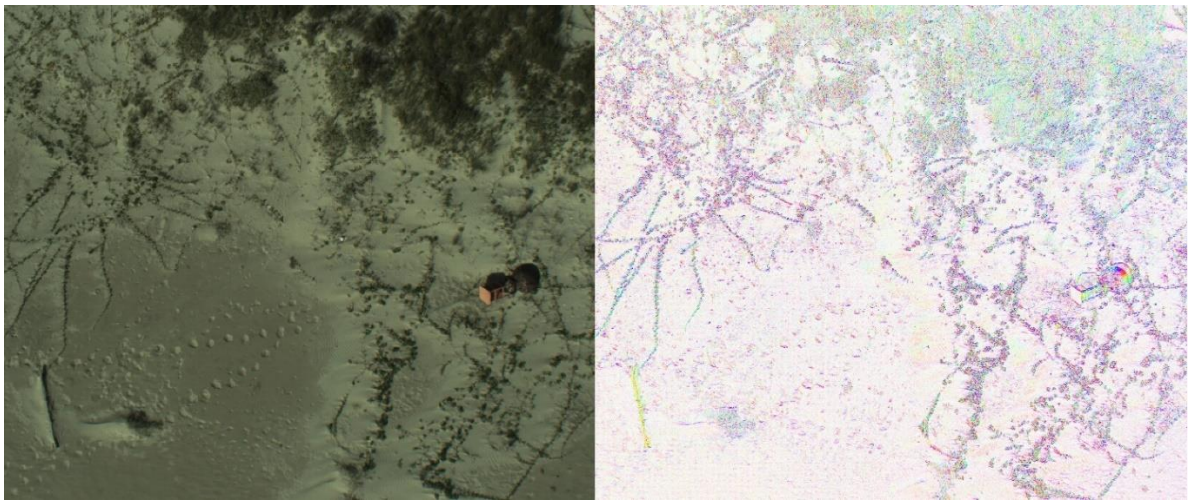

Figure 14. Metal mooring buoy @ 45m altitude, San José TX.

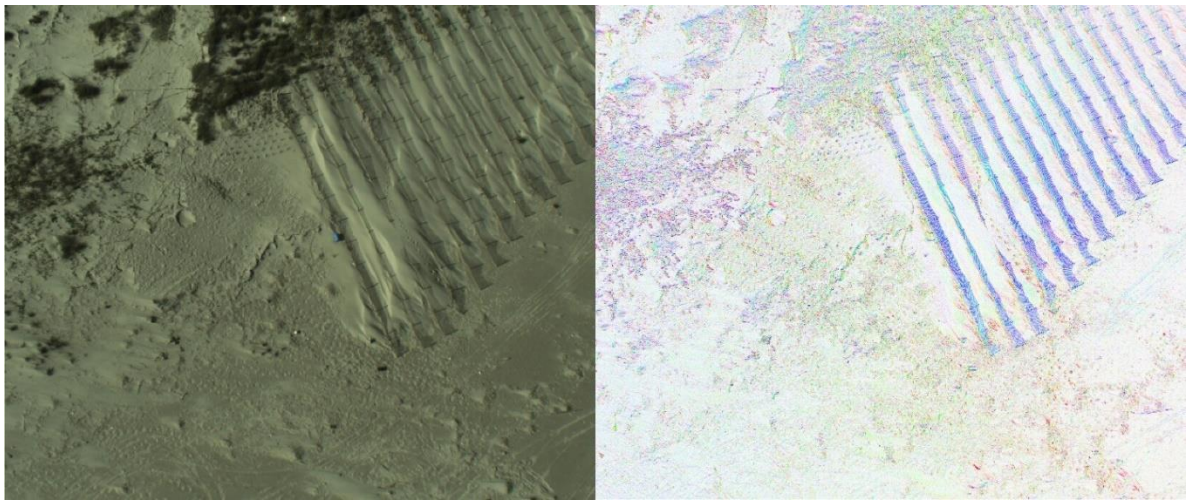

Figure 15. Partially buried fences @ 90m altitude, San José TX.

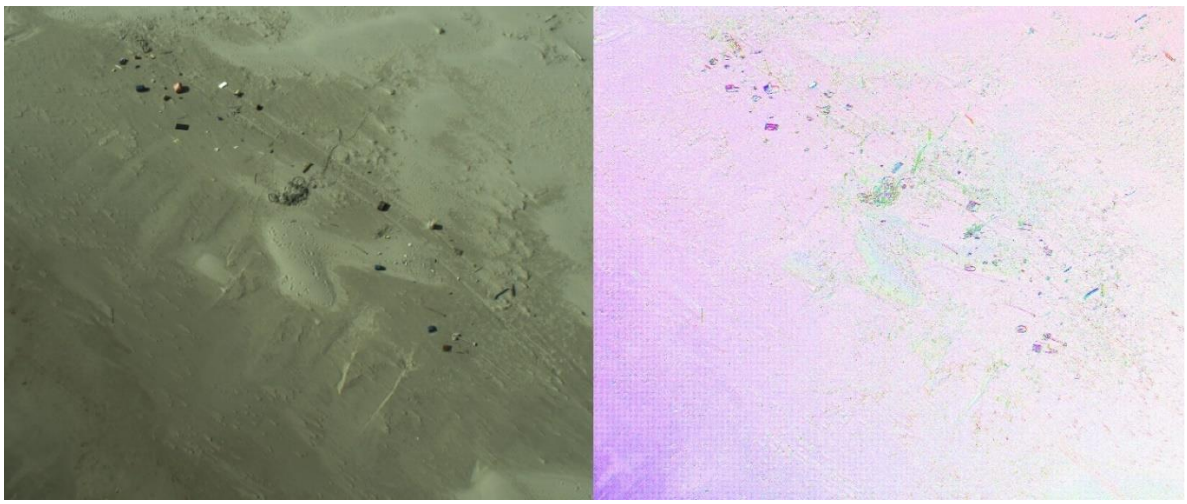

Figure 16. San José debris field 2 @ 45m altitude.

4.2. Quantitative Analysis

The classification results are expressed using training and test accuracies (per class), training and test accuracies (overall), as well as the kappa statistic. Overall accuracy is a popular classification measure that is calculated by dividing the total correct pixels (sum of the diagonal) by the total number in the error matrix. The individual class performance is measured using producer's and user's accuracies. Producer's accuracy refers to the probability of a reference pixel being correctly classified while the user's accuracy indicates the probability that a pixel on the image actually represents that class on the ground (Congalton, 1991). Kappa represents the proportion between actual agreement and the agreement expected by chance (Cohen, 1960).

$$K = \frac{(p_o - p_c)}{(1 - p_c)} \tag{11}$$

where p_o is the proportion of units in which the model agreed, and p_c is the proportion of units for which agreement is expected by chance.

The results of the band correlation analysis are shown in Tables 2, 5, and 8 for the scenes shown in Figs. 16-18. The results of the KNN classification routines are shown in Tables 3, 4, 6, 7, 9, and 10.

4.2.1. San José Orthomosaic 1

Figure 17. San José debris field 1, used for evaluating band correlations and debris classification. 5m AGL sensor height, 8 images total.

Table 2. Covariance and correlation matrices for 8-band image orthomosaic (R/G/B/S0/S1/S2/DoLP/AoLP).

SJ Ortho 1 Covariance Matrix

Layer	Red	Green	Blue	S0	S1	S2	DOLP	AOLP
Red	2544	2450	2458	2563	2579	2562	2325	1023
Green	2450	2436	2432	2524	2407	2397	2159	952
Blue	2458	2432	2634	2580	2961	2957	2738	1157
S0	2563	2524	2580	2701	2689	2678	2427	1064
S1	2579	2407	2961	2689	4837	4810	4656	2052
S2	2562	2397	2957	2678	4810	4819	4651	2094
DOLP	2325	2159	2738	2427	4656	4651	4583	2033
AOLP	1023	952	1157	1064	2052	2094	2033	7827

SJ Ortho 1 Correlation Matrix

Layer	Red	Green	Blue	S0	S1	S2	DOLP	AOLP
Red	1.000	0.984	0.950	0.978	0.735	0.732	0.681	0.229
Green	0.984	1.000	0.960	0.984	0.701	0.700	0.646	0.218
Blue	0.950	0.960	1.000	0.967	0.830	0.830	0.788	0.255
S0	0.978	0.984	0.967	1.000	0.744	0.742	0.690	0.231
S1	0.735	0.701	0.830	0.744	1.000	0.996	0.989	0.333
S2	0.732	0.700	0.830	0.742	0.996	1.000	0.990	0.341
DOLP	0.681	0.646	0.788	0.690	0.989	0.990	1.000	0.339
AOLP	0.229	0.218	0.255	0.231	0.333	0.341	0.339	1.000

Table 3. Classification results from MultiSpec K-NN analysis for SJ orthomosaic 1.

RGB (3-band)					
Material Type	Training Accuracy (Prod, user) %	Test Accuracy (Prod, user) %	Overall/kappa train (%)	Overall/kappa test (%)	Mean TD
Synthetic Rubber	91.2, 79	91.6, 71.3	83.3, 72.7	76.2, 59.1	1081
Glass	38.5, 34.4	10.8, 11.5			
Wood	78, 64.7	25.6, 21.9			
Buoy/Foam	72.4, 80.8	56.6, 45.4			
Aluminum	32.1, 67.5	3.9, 9.2			
Substrate	88.6, 93.3	84.3, 94.6			
RGB + S0 + S1 + S2 + DOLP + AOLP (8-band)					
Material Type	Training Accuracy (Prod, user) %	Test Accuracy (Prod, user) %	Overall/kappa train (%)	Overall/kappa test (%)	Mean TD
Synthetic Rubber	89.6, 86.6	90.1, 74	89.9, 82.6	82.5, 67.4	1531
Glass	30.6, 62.3	10.2, 24.4			
Wood	87.8, 87	20.7, 33.4			
Buoy/Foam	76.2, 85.2	57.9, 55.8			
Aluminum	47.2, 68.7	5.3, 8.3			
Substrate	97.2, 92.9	95.1, 93.5			

Table 4. Percentage point change of classification accuracy with the inclusion of PI-derived image bands for SJ orthomosaic 1.

Class	**Percentage Point Change Producer's Accuracy (Train, Test)**	**Percentage Point Change User's Accuracy (Train, Test)**
Synthetic Rubber	-1.6, -1.5	+7.6, +2.7
Glass	-7.9, -0.6	+27.9, +12.9
Wood	+9.8, -4.9	+22.3, +11.5
Buoy/foam	+3.8, +1.3	+4.4, +10.4
Aluminum	+15.1, +1.4	+1.2, -0.9
Substrate	+8.6, +10.8	-0.4, -0.9

4.2.2. San José Orthomosaic 2

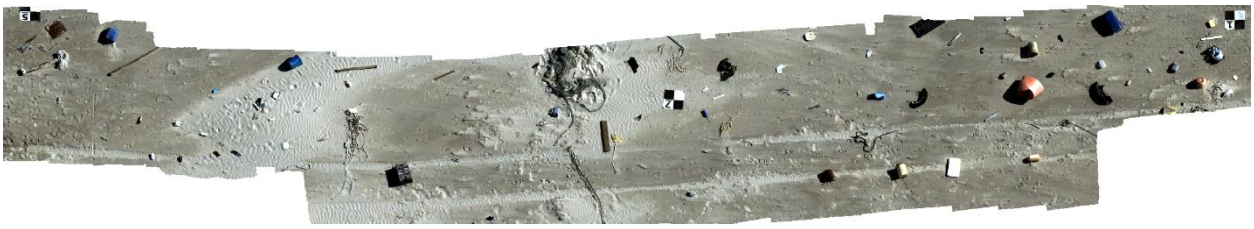

Figure 18. San José debris field 2, used for evaluating band correlations and debris classification. 4.4m AGL sensor height, 72 images total.

Table 5. Covariance and correlation matrices for 8-band image orthomosaic (R/G/B/S0/S1/S2/DoLP/AoLP).

SJ Ortho 2 Covariance Matrix

Layer	Red	Green	Blue	S0	S1	S2	DOLP	AOLP
Red	5590	5316	6235	5870	9173	9177	8870	4090
Green	5316	5076	5941	5596	8679	8684	8387	3871
Blue	6235	5941	7024	6573	10398	10407	10071	4621
S0	5870	5596	6573	6202	9662	9668	9342	4303
S1	9173	8679	10398	9662	15919	15929	15475	7073
S2	9177	8684	10407	9668	15929	15947	15489	7099
DOLP	8870	8387	10071	9342	15475	15489	15076	6893
AOLP	4090	3871	4621	4303	7073	7099	6893	7002

SJ Ortho 2 Correlation Matrix

Layer	Red	Green	Blue	S0	S1	S2	DOLP	AOLP
Red	1.000	0.998	0.995	0.997	0.972	0.972	0.966	0.654
Green	0.998	1.000	0.995	0.997	0.965	0.965	0.959	0.649
Blue	0.995	0.995	1.000	0.996	0.983	0.983	0.979	0.659
S0	0.997	0.997	0.996	1.000	0.972	0.972	0.966	0.653
S1	0.972	0.965	0.983	0.972	1.000	1.000	0.999	0.670
S2	0.972	0.965	0.983	0.972	1.000	1.000	0.999	0.672
DOLP	0.966	0.959	0.979	0.966	0.999	0.999	1.000	0.671
AOLP	0.654	0.649	0.659	0.653	0.670	0.672	0.671	1.000

Table 6. Classification results from MultiSpec K-NN analysis for SJ orthomosaic 2.

RGB (3-band)					
Material Type	Training Accuracy (Prod, user) %	Test Accuracy (Prod, user) %	Overall/kappa train (%)	Overall/kappa test (%)	Mean TD
Plastic	92.2, 71.4	50.5, 79.8	64.5, 50.4	50.1, 34.2	1213
Wood	68.5, 25.7	53.2, 13.7			
Rope	72.5, 62.7	64.9, 25.7			
Substrate	55, 94.3	45.6, 89.8			
RGB + S0 + S1 + S2 + DOLP + AOLP (8-band)					
Material Type	Training Accuracy (Prod, user) %	Test Accuracy (Prod, user) %	Overall/kappa train (%)	Overall/kappa test (%)	Mean TD
Plastic	91.5, 89.7	57.8, 93.2	89.9, 83.1	75.8, 63.5	1748
Wood	71.4, 81.1	53.4, 48.7			
Rope	81.4, 83.9	77, 39.1			
Substrate	95.9, 93.3	90.7, 90.4			

Table 7. Percentage point change of classification accuracy with the inclusion of PI-derived image bands for SJ orthomosaic 2.

Class	**Percentage Point Change Producer's Accuracy (Train, Test)**	**Percentage Point Change User's Accuracy (Train, Test)**
Plastic	-0.7, +7.3	+18.3, +13.4
Wood	+2.9, +0.2	+55.4, +35
Rope	+8.9, +12.1	+31.2, +13.4
Substrate	+40.9, +45.1	-1, +0.6

4.2.3. Wavelab Orthomosaic

Figure 19. Wavelab debris field, used for evaluating band correlations and debris classification. 3.6m AGL sensor height, 34 images total.

Table 8. Covariance and correlation matrices for 8-band image orthomosaic (R/G/B/S0/S1/S2/DoLP/AoLP).

Wavelab Ortho Covariance Matrix

Layer	Red	Green	Blue	S0	S1	S2	DOLP	AOLP
Red	9345	9228	9451	8213	9821	9877	8295	5395
Green	9228	9239	9495	8216	9734	9806	8217	5399
Blue	9451	9495	9944	8233	10381	10483	8841	5721
S0	8213	8216	8233	7951	8012	8036	6591	4580
S1	9821	9734	10381	8012	11943	12043	10410	6529
S2	9877	9806	10483	8036	12043	12182	10507	6653
DOLP	8295	8217	8841	6591	10410	10507	9359	5833
AOLP	5395	5399	5721	4580	6529	6653	5833	9615

Wavelab Ortho Correlation Matrix

Layer	Red	Green	Blue	S0	S1	S2	DOLP	AOLP
Red	1.000	0.993	0.980	0.953	0.930	0.926	0.887	0.569
Green	0.993	1.000	0.991	0.959	0.927	0.924	0.884	0.573
Blue	0.980	0.991	1.000	0.926	0.953	0.952	0.916	0.585
S0	0.953	0.959	0.926	1.000	0.822	0.817	0.764	0.524
S1	0.930	0.927	0.953	0.822	1.000	0.998	0.985	0.609
S2	0.926	0.924	0.952	0.817	0.998	1.000	0.984	0.615
DOLP	0.887	0.884	0.916	0.764	0.985	0.984	1.000	0.615
AOLP	0.569	0.573	0.585	0.524	0.609	0.615	0.615	1.000

Table 9. Classification results from MultiSpec K-NN analysis for wavelab orthomosaic.

RGB (3-band)					
Material Type	Training Accuracy (Prod, user) %	Test Accuracy (Prod, user) %	Overall/kappa train (%)	Overall/kappa test (%)	Mean TD
Plastic	92.4, 50.3	55.9, 32.8	71.9, 60.5	51.8, 33.2	1219
Glass	16.7, 28.8	3.4, 4.7			
Buoy/foam	87.1, 68.8	37.1, 38.4			
Other Debris	65.7, 79.1	49.3, 59.1			
Substrate	66.3, 91.6	57.6, 74.8			
RGB + S0 + S1 + S2 + DOLP + AOLP (8-band)					
Material Type	Training Accuracy (Prod, user) %	Test Accuracy (Prod, user) %	Overall/kappa train (%)	Overall/kappa test (%)	Mean TD
Plastic	86.7, 81.7	38.1, 49.5	86.9, 80.8	64.2, 48.2	1639
Glass	19.9, 69.5	2.2, 6.5			
Buoy/foam	89.8, 92	40.1, 40.5			
Other Debris	88.6, 85.7	74.9, 65.2			
Substrate	86.6, 90.8	76.6, 76.7			

Table 10. Percentage point change of classification accuracy with the inclusion of PI-derived image bands for Wavelab orthomosaic.

Class	**Percentage Point Change Producer's Accuracy (Train, Test)**	**Percentage Point Change User's Accuracy (Train, Test)**
Plastic	-5.7, -16	+31.4, +17.7
Glass	+3.2, -1.2	+40.7, +1.8
Buoy/foam	+2.7, +3	+23.2, +2.1
Other Debris	+22.9, +25.6	+6.6, +6.1
Substrate	+20.3, +19	-0.8, +1.9

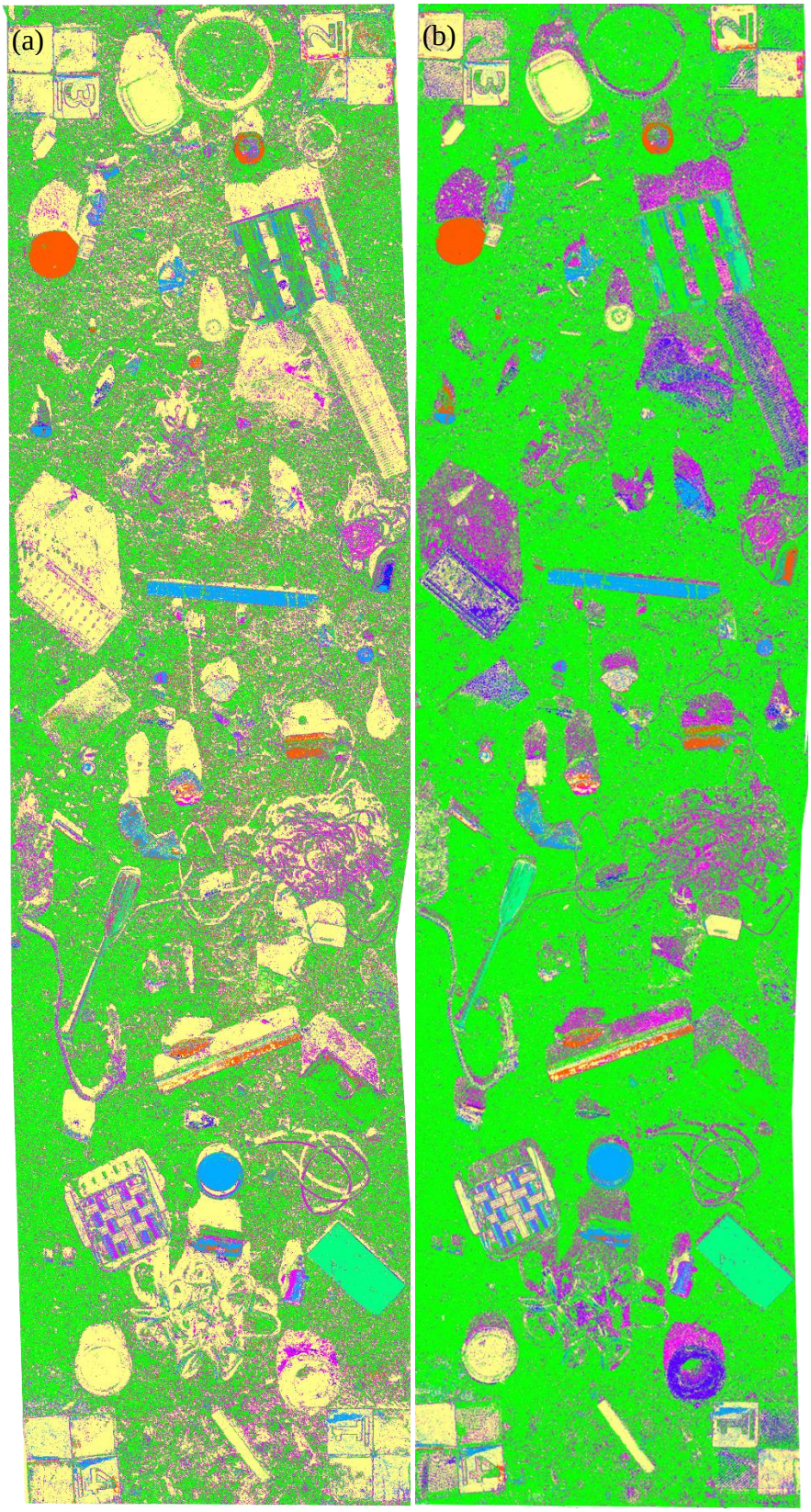

Figure 20. (a-b) Wavelab ortho surface cluster mask results from KNN algorithm. (a) RGB (left); (b) 8-band (right).

5. Discussion

Beyond the overall accuracy assessment results, the transformed divergence (TD) values were found to provide insight into the improvement attainable by adding the PI information. The TD values substantially increased, indicating that polarimetric inclusion benefits separability of marine debris classes. This is likely attributed to the added information about surface texture features such as roughness, shape, and shading. The TD results revealed that red-green-blue were not always the best 3-band combination for debris separability within these scenes. For the SJ ortho 1, the best 3-band combination was green-blue-S0 with an average TD value of 1175 (versus 1081 RGB). For SJ ortho 2, the best combination was red-blue-S0 at 1366 (versus 1213 for RGB). The wavelab ortho best 3-band combination was indeed red-green-blue with an average TD value of 1219. As a specific example, if we consider the SJ Ortho 2 and the separability of plastic vs. rope, the TD value when using only the RGB bands is 560, which is considered very poor (inseparable). However, by adding the PI-derived bands, the TD jumps to 1546. Similarly, if we consider wood vs. rope for the same orthomosaic, the TD value for RGB only was 662, but increased to 1561 after adding the PI-derived bands. These results are particularly interesting for future studies in evaluating the ideal data combinations in debris classification procedures.

On the USCG helicopter, the FLIR camera performed well at altitudes of up to 90 meters and speeds of 8 m/s once the exposure was adjusted accordingly. The quality of the aerial imagery obtained showed promise for implementing this type of technology in debris survey and response efforts. Future efforts could benefit from use of a Raspberry Pi onboard system to increase autonomous camera function and allow full UAS integration. Polarimetric sensor technology of this size has only been released to market within the last decade and is certain to be further developed as its field applications continue to grow.

The investigations performed in this study identified practical challenges and technological limitations of the system employed. The lack of camera autonomy, primarily due to the new sensors, meant that the acquisition process was quite manual and tedious. The camera required consistent cable connection to a field laptop where images were individually captured, and parameters often adjusted. Exposure level and weather conditions were key for polarimetric imaging quality. Time of day/incidence angle substantially affected polarimetric state observed

on many objects tested where the same object resulted in different reflectance signatures between scenes. Atmospheric conditions also significantly affected the polarized light state observed. Yan et al. (2020) found that dense or even partial cloud cover induced a light scattering phenomenon which decreases quality of both DoLP and AoLP. Shoreline and substrate conditions also heavily influenced debris detection and classification. Objects nestled in dense vegetation or submerged in complex substrate (i.e. rocks/shells/sand) were not easily identifiable in the polarimetric imagery. Wet sand and compacted features, such as footprints and car tracks, also showed polarimetric returns and added noise to some scenes.

6. Conclusion

This study provided strong indication that polarimetric imaging is a useful asset in detection and classification of marine debris objects across seven material classes. Overall, the polarimetric information displayed visually rich object characteristics and improved both the visual identification and automated classification of debris. In particular, polarimetric imaging enhanced information about surface textures, shape, shading, and roughness that spectral bands otherwise could not.

A major logistical challenge was sourcing sufficient debris accumulations of various material types. Most scenes and debris encountered consisted of primarily plastic objects, followed by processed wood, buoys/foam, glass, rubber, ropes/nets, and aluminum cans. Due to the practical limitations of the field study (particularly, the number and types of debris items available and amount of area that could realistically be covered using the pole-mounted camera), the sampling strategy and numbers of items sampled within each class did not adhere to the stringent guidelines often employed in remote sensing for classification accuracy assessment (e.g., Congalton and Green, 2019). For this reason, the accuracy values in Tables 3, 6 and 9 may overestimate the accuracies that could be achieved in an operational marine debris mapping project. However, what is important in these tables is the *improvement* in accuracy, based on adding the PI-derived bands.

Future endeavors can build on this work by experimenting with different material types and machine learning algorithms. One recommended extension is to investigate other machine learning algorithms, beyond KNN, for auto-classification of debris in the imagery. For example, convolutional neural networks could be investigated for classification of marine debris in polarimetric imagery, where much larger training data sets are available. It would also be advantageous to acquire imagery at variable incidence angles and sky conditions to investigate optimal acquisition conditions and parameters.

Integration of polarimetric sensors on UAS platforms would greatly expand operational capabilities and could easily be employed for coastal response teams such as NOAA's Marine Debris Program. Hence, future efforts should focus on integrating the PI camera onto a UAS, leveraging the work done in this study acquiring imagery from the helicopter. Lastly, it would be of interest to investigate additional methods of processing the PI data for both enhanced visual

analysis and use in the automated classification routines. Through this ongoing work, PI cameras are anticipated to become increasingly valuable for the application of marine debris detection and classification.

References

Bamford, H.A., 2013. *Programmatic environmental assessment for the NOAA Marine Debris Program*. National Oceanic and Atmospheric Administration, Department of Commerce, Silver Spring, Maryland.

Brooke, S., Graham, D., Jacobs, T., Littnan, C., Manuel, M., & O'Conner, R. (2015). Testing marine conservation applications of Unmanned Aerial Systems (UAS) in a Remote Marine Protected Area. *Journal of Unmanned Vehicle Systems*, *3*(4), 237–251. https://doi.org/10.1139/juvs-2015-0011

Burgess, H.K., Herring C.E., Lippiatt S., Lowe S., & Uhrin A.V. (2021). *NOAA Marine Debris Monitoring and Assessment Project Shoreline Survey Guide*. NOAA Technical Memorandum NOS OR&R 56. 20 pp. DOI 10.25923/g720-2n18

Gonçalves, G., Andriolo, U., Pinto, L., & Bessa, F. (2020). Mapping marine litter using UAS on a beach-dune system: A multidisciplinary approach. *Science of The Total Environment*, *706*, 135742. https://doi.org/10.1016/j.scitotenv.2019.135742

Opfer, S., Arthur, C. and Lippiatt, S., 2012. *NOAA Marine Debris Shoreline Survey Field Guide*. National Oceanic and Atmospheric Administration, Department of Commerce, Silver Spring, Maryland.

Snik, F., Craven-Jones, J., Escuti, M., Fineschi, S., Harrington, D., De Martino, A., Mawet, D., Riedi, J., & Tyo, J. S. (2014). An overview of polarimetric sensing techniques and technology with applications to different research fields. *SPIE Proceedings*. https://doi.org/10.1117/12.2053245

Taddia, Y., Corbau, C., Buoninsegni, J., Simeoni, U., & Pellegrinelli, A. (2021). UAV approach for detecting plastic marine debris on the beach: A case study in the Po River Delta (Italy). *Drones*, *5*(4), 140. https://doi.org/10.3390/drones5040140

Tyo, J. S., Goldstein, D. L., Chenault, D. B., & Shaw, J. A. (2006). Review of passive imaging polarimetry for Remote Sensing Applications. *Applied Optics*, *45*(22), 5453. https://doi.org/10.1364/ao.45.005453

Yan, L., Chen, W., Zhang, F., Yang, B., & Xiang, Y. (2020). *Polarization Remote Sensing Physics*. Springer.

Chauhan, S., & Srivastava, H. S. (2016). Comparative Evaluation of the Sensitivity of Multi-Polarised SAR and Optical Data for Various Land Cover Classes. *International Journal of Advancement in Remote Sensing, GIS and Geography*, *4*(1).

Sawaya, S., Haack, B., Idol, T., & Sheoran, A. (2010). Land use/cover mapping with quad-polarization radar and derived texture measures near Wad Madani, Sudan. *GIScience & Remote Sensing*, *47*(3), 398–411. https://doi.org/10.2747/1548-1603.47.3.398

Islam, M. N., Tahtali, M., & Pickering, M. (2019). Man-made object separation using polarimetric imagery. *SPIE Future Sensing Technologies*. https://doi.org/10.1117/12.2547475

Zhao, Y.-Q., Gong, P., & Pan, Q. (2008). Object detection by spectropolarimeteric imagery fusion. *IEEE Transactions on Geoscience and Remote Sensing*, *46*(10), 3337–3345. https://doi.org/10.1109/tgrs.2008.920467

Mausel, P. W., Kramber, W. J., & Lee, J. K. (1990). Optimum Band Selection for Supervised Classification of Multispectral Data. *Photogrammetric Engineering and Remote Sensing*, *56*(1), 55–60.

Stokes, G. G. (1852). *On the composition and resolution of streams of polarized light from different sources*. Printed at the Pitt Press by John W. Parker.

Sheavly, S. B., & Register, K. M. (2007). Marine Debris & Plastics: Environmental concerns, sources, impacts and solutions. *Journal of Polymers and the Environment*, *15*(4), 301–305. https://doi.org/10.1007/s10924-007-0074-3

Biehl, L., & Landgrebe, D. (2002). MultiSpec—a tool for multispectral–Hyperspectral Image Data Analysis. *Computers & Geosciences*, *28*(10), 1153–1159. https://doi.org/10.1016/s0098-3004(02)00033-x

Pawar, P., & Shirgaonkar, S. (2016). Plastic Marine Debris: Sources, Distribution and Impacts on Coastal and Ocean Biodiversity. *Journal of Biological Sciences*, *3*(1), 40–54.

Save time and effort with on-sensor polarization. Imaging Reflective Surfaces: Sony's first Polarized Sensor | Teledyne FLIR. (n.d.). Retrieved January 3, 2022, from https://www.flir.com/discover/iis/machine-vision/imaging-reflective-surfaces-sonys-first-polarized-sensor/

Congalton, R. G., & Green, K. (2019). *Assessing the accuracy of remotely sensed data: Principles and practices*. CRC Press.

Conte, C., de Alteriis, G., DePandi, F., Lo Moriello, R. S., Rufino, G., & Accardo, D. (2021). Integration of a sun light polarization camera and latest-generation inertial sensors to support high integrity navigation. *2021 28th Saint Petersburg International Conference on Integrated Navigation Systems (ICINS)*. https://doi.org/10.23919/icins43216.2021.9470796

Congalton, R. G. (1991). A review of assessing the accuracy of classifications of remotely sensed data. *Remote Sensing of Environment*, *37*(1), 35–46. https://doi.org/10.1016/0034-4257(91)90048-b

Cohen, J. (1960). A coefficient of agreement for nominal scales. *Educational and Psychological Measurement*, *20*(1), 37–46. https://doi.org/10.1177/001316446002000104

Silverman, B. W., & Jones, M. C. (1989). E. Fix and J.L. Hodges (1951): An Important Contribution to Nonparametric Discriminant Analysis and Density Estimation: Commentary on Fix and Hodges (1951). *International Statistical Review / Revue Internationale de Statistique*, *57*(3), 233–238. https://doi.org/10.2307/1403796

Appendix A: RGB vs Bivariate Image Examples

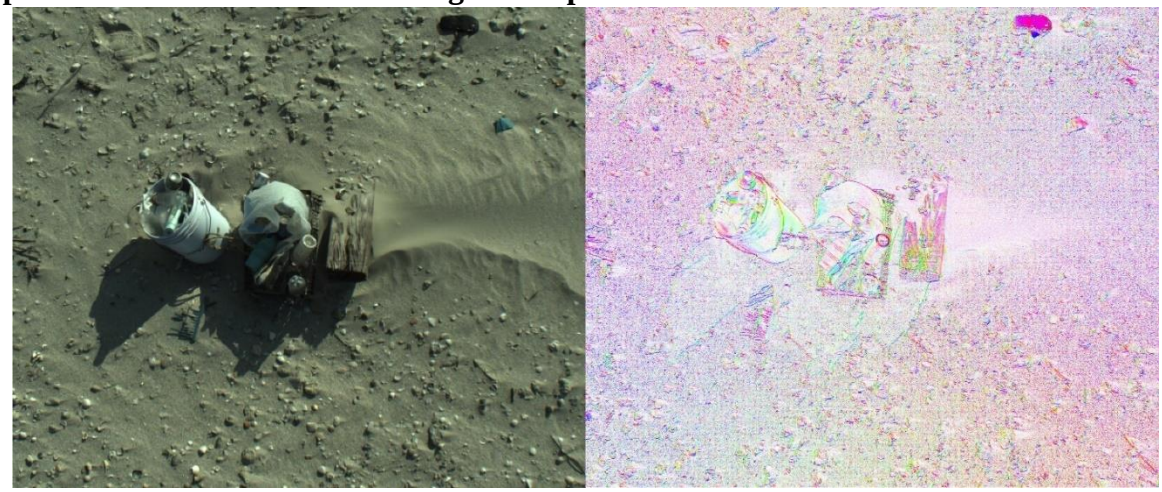

Figure A.1. Pile of trash, San José TX.

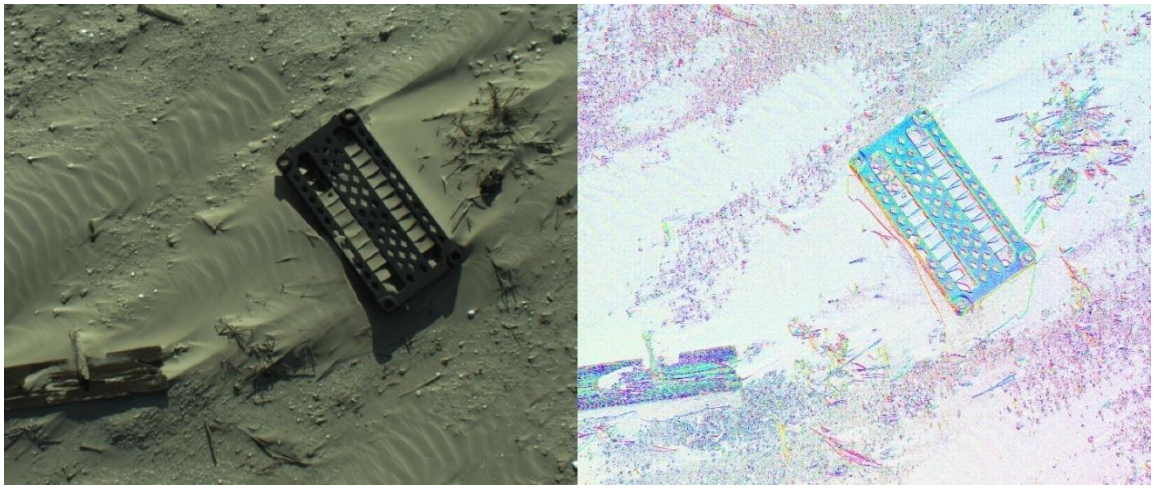

Figure A.2. Plastic crate and wood fragment partially buried, San José TX.

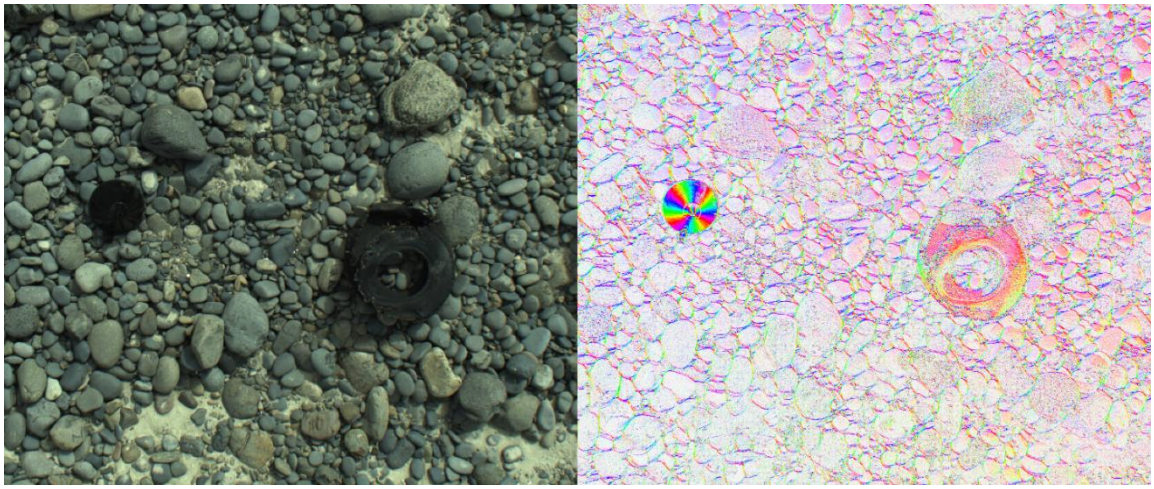

Figure A.3.Tire fragment and plastic funnel on cobblestone, Neptune OR.

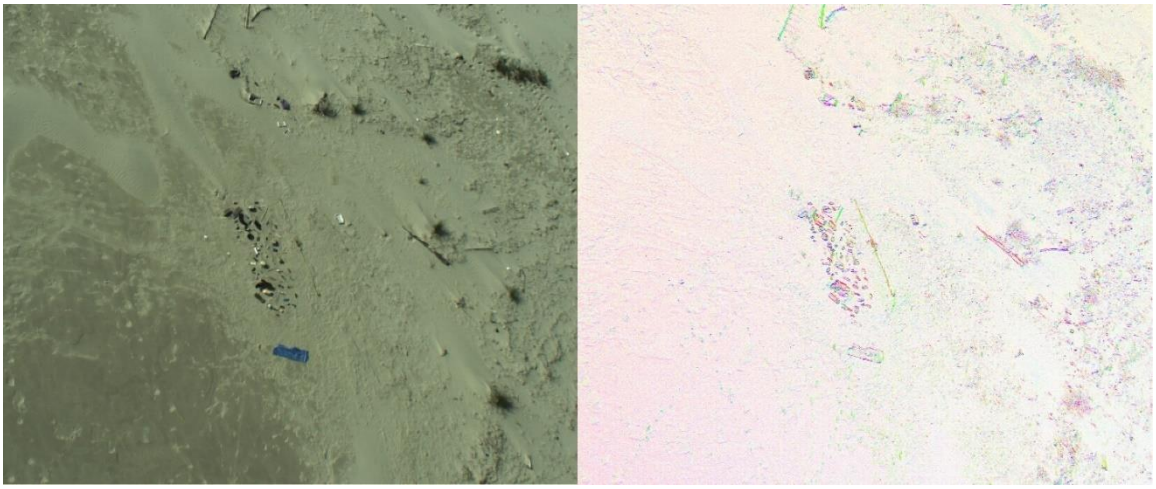

Figure A.4. San José debris field 1 @ 45m altitude.

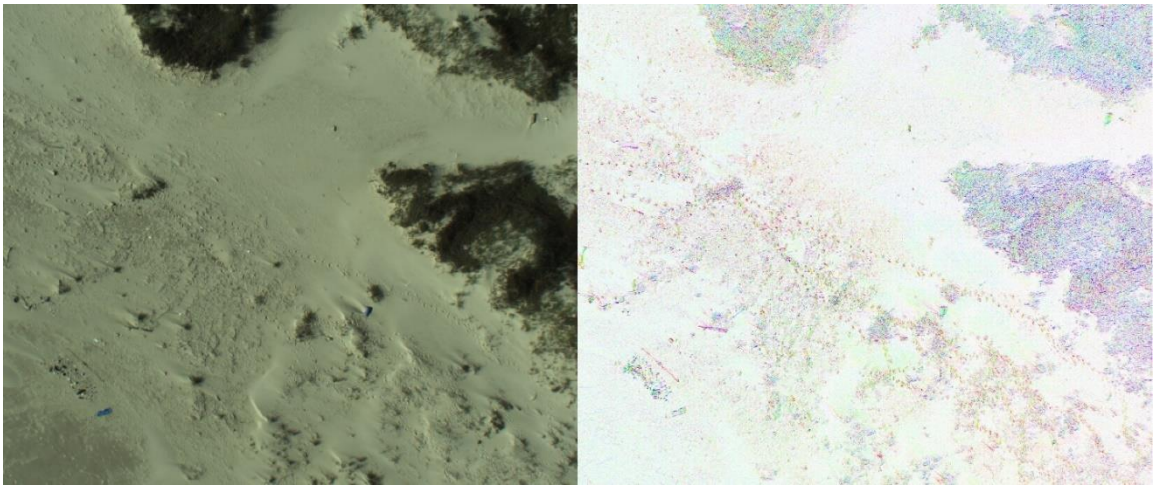

Figure A.5. San José debris field 1 @ 90m altitude.

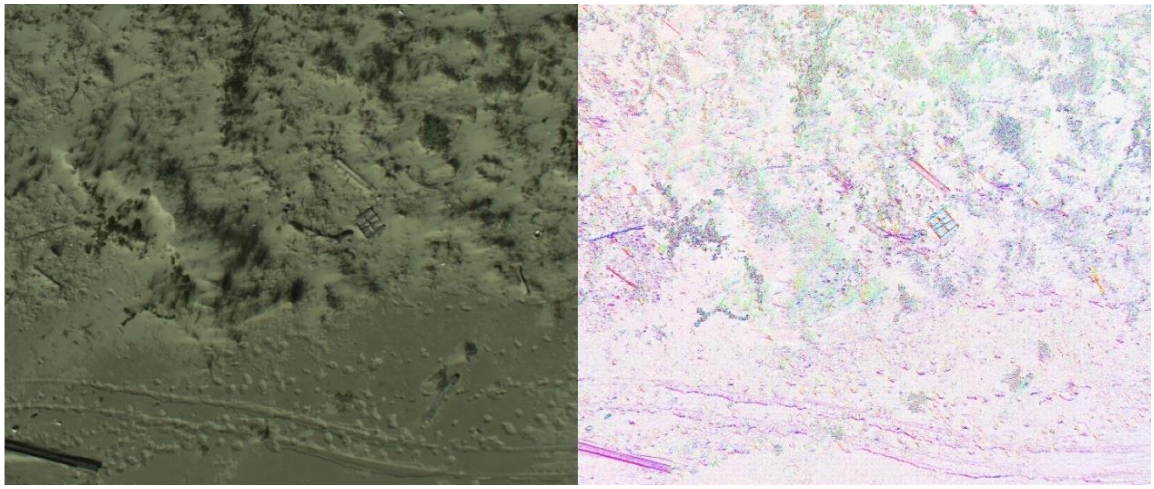

Figure A.6. Processed wood debris @ 45m altitude, San José TX.

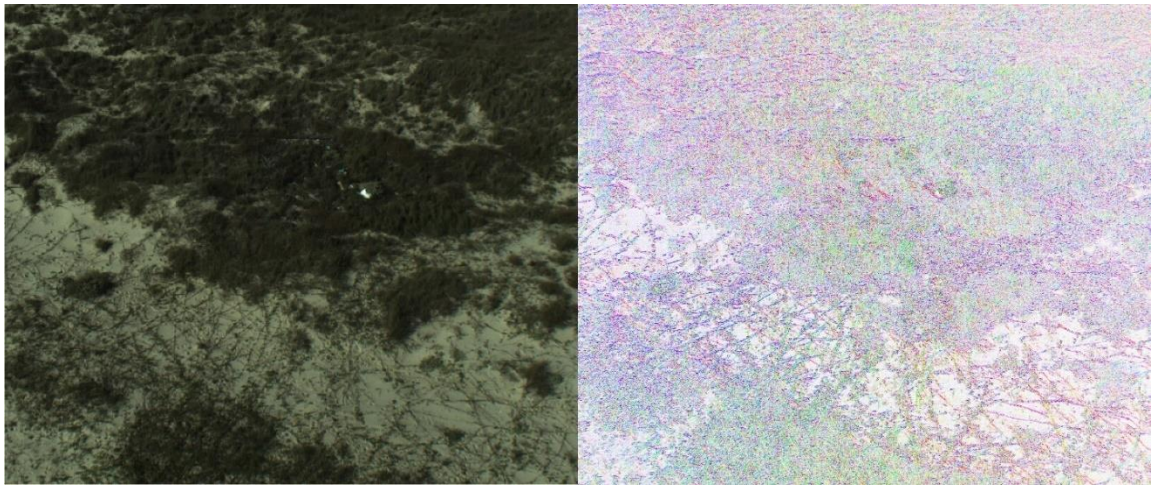

Figure A.7. Scattered debris in dense vegetation @ 45m altitude, San José TX.

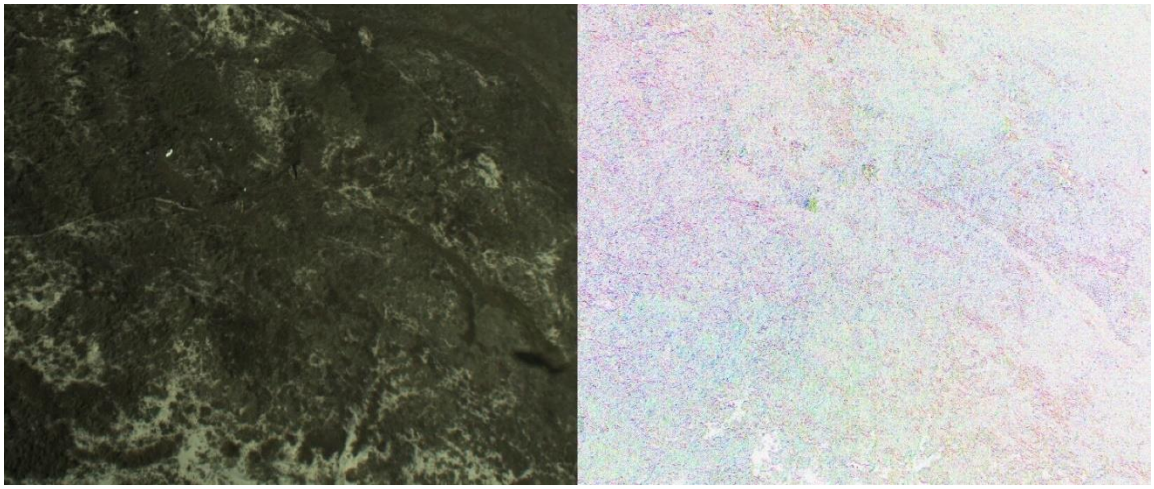

Figure A.8. Scattered debris in dense vegetation @ 90m altitude, San José TX.

Appendix B: Transformed Divergence Results

Table B.1. Transformed divergence results for San José Orthomosaic 1, sorted by best average value across all classes.

SJ Ortho 1 Transformed Divergence Results - Best band combinations for interclass separability																		
Best 3-band Combinations			class pairs >	Rubber vs Glass	Rubber vs Wood	Rubber vs Foam	Rubber vs Aluminum	Rubber vs Substrate	Glass vs Wood	Glass vs Foam	Glass vs Aluminum	Glass vs Substrate	Wood vs Foam	Wood vs Aluminum	Wood vs Substrate	Foam vs Aluminum	Foam vs Substrate	Aluminum vs Substrate
			weighting factor >	10	10	10	10	10	10	10	10	10	10	10	10	10	10	10
Rank	**Channels**	**Min.**	**Average**	**Weighted Interclass Distance Measures**														
1	2 3 4	200	1175	1070	1257	1823	1260	1959	200	889	461	1290	1054	459	1254	770	1995	1888
2	1 4 6	299	1131	985	1421	1777	1161	1860	497	845	299	1061	878	736	1487	338	1962	1666
3	2 4 6	247	1131	1026	1458	1811	1218	1914	492	835	247	1066	842	732	1505	257	1969	1591
4	2 3 6	443	1107	879	1292	1307	767	1828	443	637	499	1144	1088	842	1489	690	1941	1765
5	1 3 4	122	1104	908	1178	1784	1234	1931	122	881	384	1219	795	428	1158	713	1980	1836
6	1 2 3	398	1081	810	931	1366	778	1859	398	814	429	1152	1445	569	1002	899	1974	1786
7	3 4 6	268	1076	690	1330	1722	1135	1697	483	841	268	1016	901	786	1506	303	1960	1510
8	1 2 4	71	1060	956	1218	1799	1231	1939	71	880	263	1145	755	339	1026	571	1977	1730
9	1 3 6	399	1060	699	1234	1288	730	1763	399	732	406	1109	936	817	1481	716	1891	1690
10	1 4 7	256	1051	895	1217	1764	1191	1873	322	845	256	1021	686	460	1205	381	1967	1678
Best 4-band Combinations																		
Rank	**Channels**	**Min.**	**Average**	**Weighted Interclass Distance Measures**														
1	2 3 4 6	543	1325	1191	1522	1837	1296	1964	629	954	543	1392	1226	935	1694	799	1995	1895
2	1 2 3 4	470	1276	1111	1340	1838	1293	1968	470	978	472	1402	1493	642	1296	925	1997	1908
3	1 3 4 6	466	1267	1041	1486	1801	1268	1937	554	947	466	1338	1018	898	1668	745	1982	1848
4	2 3 4 5	426	1260	1208	1308	1842	1300	1965	426	948	547	1434	1119	570	1508	822	1996	1903
5	2 3 4 7	461	1252	1122	1357	1831	1308	1967	461	962	492	1370	1090	623	1496	810	1996	1901
8-band Combination																		
Rank	**Channels**	**Min.**	**Average**	**Weighted Interclass Distance Measures**														
1	1 to 8	667	1531	1462	1790	1895	1458	1980	1136	1176	667	1609	1716	1259	1802	1081	1998	1934

Table B.2. Transformed divergence results for San José Orthomosaic 2, sorted by best average value across all classes.

SJ Ortho 2 Transformed Divergence Results - Best band combinations for interclass separability										
Best 3-band Combinations			class pairs >	Plastic vs Wood	Plastic vs Rope	Plastic vs Substrate	Wood vs Rope	Wood vs Substrate	Rope vs Substrate
			weighting factor >	10	10	10	10	10	10
Rank	**Channels**	**Min.**	**Average**	**Weighted Interclass Distance Measures**					
1	1 3 4	697	1366	1947	697	1972	852	1280	1447
2	2 3 4	688	1321	1892	688	1970	706	1242	1429
3	1 4 7	768	1316	1805	960	1646	768	1240	1478
4	1 2 4	499	1312	1906	499	1869	913	1277	1407
5	2 4 7	763	1285	1795	939	1529	763	1212	1469
6	3 4 7	570	1264	1633	956	1719	570	1193	1514
7	1 4 6	689	1258	1786	689	1631	953	1188	1302
8	1 3 7	543	1248	1446	988	1932	543	1004	1573
9	2 3 7	480	1242	1386	1013	1940	480	1067	1563
10	1 4 5	582	1232	1804	582	1659	692	1275	1379
11	2 4 6	659	1224	1775	659	1504	962	1156	1290
12	1 2 3	560	1213	1519	560	1968	662	1097	1472
Best 4-band Combinations									
Rank	**Channels**	**Min.**	**Average**	**Weighted Interclass Distance Measures**					
1	1 3 4 7	991	1515	1955	1144	1974	991	1334	1694
2	1 3 4 6	933	1481	1949	933	1976	1141	1294	1594
3	2 3 4 7	871	1480	1906	1147	1972	871	1299	1682
4	1 2 4 7	1018	1477	1917	1018	1879	1046	1328	1670
5	1 2 3 4	771	1461	1955	771	1986	1059	1367	1627
8-band Combination									
Rank	**Channels**	**Min.**	**Average**	**Weighted Interclass Distance Measures**					
1	1 to 8	1521	1748	1975	1546	1994	1561	1521	1894

Table B.3. Transformed divergence results for Wavelab Orthomosaic, sorted by best average value across all classes.

Wavelab Ortho Transformed Divergence Results - Best band combinations for interclass separability														
Best 3-band Combinations			class pairs >	Plastic vs Glass	Plastic vs Foam	Plastic vs Other	Plastic vs Substrate	Glass vs Foam	Glass vs Other	Glass vs substrate	Foam vs Other	Foam vs Substrate	Other vs substrate
			weighting factor >	10	10	10	10	10	10	10	10	10	10
Rank	**Channels**	**Min.**	**Average**	**Weighted Interclass Distance Measures**									
1	1 2 3	371	1219	874	1996	692	957	1324	371	1068	1680	1995	1237
2	1 3 4	218	1206	710	1959	626	1184	1118	218	1342	1308	2000	1591
3	1 3 6	604	1169	1171	1902	616	958	1261	604	1068	890	1985	1235
4	1 3 7	560	1161	661	1942	724	878	1622	560	1021	977	1989	1241
5	1 2 4	218	1150	640	1993	705	757	1326	218	1100	1435	1998	1331
6	1 2 6	603	1146	1167	1990	687	641	1435	603	829	1171	1972	969
7	1 2 7	543	1119	655	1994	792	543	1714	553	744	1232	1980	982
8	1 3 5	337	1094	746	1918	601	882	1069	337	1128	1064	1991	1207
9	2 3 4	367	1091	691	1616	436	1186	897	367	1342	808	1999	1568
10	2 3 7	523	1073	583	1632	523	932	1503	604	1068	725	1968	1196
Best 4-band Combinations													
Rank	**Channels**	**Min.**	**Average**	**Weighted Interclass Distance Measures**									
1	1 2 3 4	522	1380	1010	1997	755	1241	1450	522	1432	1762	2000	1629
2	1 2 3 6	716	1361	1336	1996	716	1045	1541	820	1190	1689	1996	1280
3	1 3 4 6	651	1354	1241	1960	651	1248	1387	698	1429	1320	2000	1610
4	1 3 4 7	646	1343	770	1978	751	1197	1701	646	1392	1379	2000	1618
5	1 2 3 7	766	1340	925	1998	818	973	1775	766	1144	1712	1997	1291
8-band Combination													
Rank	**Channels**	**Min.**	**Average**	**Weighted Interclass Distance Measures**									
1	1 to 8	990	1639	1590	1999	990	1393	1920	1332	1637	1846	2000	1688

Appendix C: Single 8-band image band correlation examples (pre-mosaic)

Figure C.1. Single 8-band image (5/8) from San José debris field 1.

Table C.1. Covariance and correlation statistics for Fig C.1.

SJ Ortho 1 Single 8-band Covariance Matrix

Layer	Red	Green	Blue	S0	S1	S2	DOLP	AOLP
Red	1454	1435	1101	1389	26	13	-167	-16
Green	1435	1520	1189	1449	15	11	-179	-30
Blue	1101	1189	1030	1155	0	6	-136	-100
S0	1389	1449	1155	1637	16	9	-196	-61
S1	26	15	0	16	43	13	37	102
S2	13	11	6	9	13	52	44	193
DOLP	-167	-179	-136	-196	37	44	179	169
AOLP	-16	-30	-100	-61	102	193	169	16025

SJ Ortho 1 Single 8-band Correlation Matrix

Layer	Red	Green	Blue	S0	S1	S2	DOLP	AOLP
Red	1.000	0.965	0.900	0.900	0.103	0.047	-0.328	-0.003
Green	0.965	1.000	0.950	0.918	0.057	0.038	-0.343	-0.006
Blue	0.900	0.950	1.000	0.890	0.000	0.027	-0.317	-0.025
S0	0.900	0.918	0.890	1.000	0.059	0.030	-0.363	-0.012
S1	0.103	0.057	0.000	0.059	1.000	0.263	0.421	0.122
S2	0.047	0.038	0.027	0.030	0.263	1.000	0.459	0.211
DOLP	-0.328	-0.343	-0.317	-0.363	0.421	0.459	1.000	0.100
AOLP	-0.003	-0.006	-0.025	-0.012	0.122	0.211	0.100	1.000

Figure C.2. Single 8-band image (34/72) from San José debris field 2.

Table C.2. Covariance and correlation statistics for Fig C.2.

SJ Ortho 2 Single 8-band Covariance Matrix								
Layer	**Red**	**Green**	**Blue**	**S0**	**S1**	**S2**	**DOLP**	**AOLP**
Red	487	490	387	475	11	1	-60	122
Green	490	538	438	513	6	-2	-68	102
Blue	387	438	392	424	-1	-2	-54	53
S0	475	513	424	675	7	-3	-78	87
S1	11	6	-1	7	21	3	17	67
S2	1	-2	-2	-3	3	20	17	172
DOLP	-60	-68	-54	-78	17	17	68	74
AOLP	122	102	53	87	67	172	74	16020

SJ Ortho 2 Single 8-band Correlation Matrix								
Layer	**Red**	**Green**	**Blue**	**S0**	**S1**	**S2**	**DOLP**	**AOLP**
Red	1.000	0.958	0.886	0.828	0.109	0.008	-0.327	0.044
Green	0.958	1.000	0.954	0.850	0.052	-0.016	-0.357	0.035
Blue	0.886	0.954	1.000	0.824	-0.006	-0.026	-0.333	0.021
S0	0.828	0.850	0.824	1.000	0.060	-0.027	-0.362	0.026
S1	0.109	0.052	-0.006	0.060	1.000	0.158	0.442	0.116
S2	0.008	-0.016	-0.026	-0.027	0.158	1.000	0.453	0.301
DOLP	-0.327	-0.357	-0.333	-0.362	0.442	0.453	1.000	0.071
AOLP	0.044	0.035	0.021	0.026	0.116	0.301	0.071	1.000

Figure C.3. Single 8-band image (18/34) from Wavelab debris field.

Table C.3. Covariance and correlation statistics for Fig C.3.

Wavelab Ortho Single 8-band Covariance Matrix

Layer	Red	Green	Blue	S0	S1	S2	DOLP	AOLP
Red	1978	1920	1470	2495	111	43	-295	269
Green	1920	2097	1692	2625	87	43	-330	307
Blue	1470	1692	1515	2039	35	28	-292	238
S0	2495	2625	2039	4180	175	83	-490	458
S1	111	87	35	175	86	14	95	40
S2	43	43	28	83	14	54	66	224
DOLP	-295	-330	-292	-490	95	66	733	248
AOLP	269	307	238	458	40	224	248	16198

Wavelab Ortho Single 8-band Correlation Matrix

Layer	Red	Green	Blue	S0	S1	S2	DOLP	AOLP
Red	1.000	0.943	0.849	0.868	0.268	0.133	-0.245	0.048
Green	0.943	1.000	0.949	0.887	0.204	0.128	-0.266	0.053
Blue	0.849	0.949	1.000	0.810	0.097	0.098	-0.277	0.048
S0	0.868	0.887	0.810	1.000	0.292	0.174	-0.280	0.056
S1	0.268	0.204	0.097	0.292	1.000	0.202	0.378	0.034
S2	0.133	0.128	0.098	0.174	0.202	1.000	0.329	0.239
DOLP	-0.245	-0.266	-0.277	-0.280	0.378	0.329	1.000	0.072
AOLP	0.048	0.053	0.048	0.056	0.034	0.239	0.072	1.000